LA-UR- *09-0119 2*

Title: | Trends in Covalency for d– and and f–Element Metallocene Dichlorides Identified Using Chlorine K–Edge X–Ray Absorption Spectroscopy and Time Dependent–Density Functional Theory

Author(s): | Stosh A. Kozimor, Ping Yang, Enrique R. Batista, Kevin S. Boland, Carol J. Burns, David L. Clark,* Steven D. Conradson,* P. Jeffrey Hay, Richard L. Martin,* Marianne P. Wilkerson, Laura E. Wolfsberg

Intended for: | Journal of the American Chemical Society

.

> **Los Alamos**
> NATIONAL LABORATORY
> ——— EST.1943 ———

Trends in Covalency for *d*- and and *f*-Element Metallocene Dichlorides Identified Using Chlorine K–Edge X–Ray Absorption Spectroscopy and Time Dependent–Density Functional Theory

Stosh A. Kozimor, Ping Yang, Enrique R. Batista, Kevin S. Boland,
Carol J. Burns, David L. Clark,* Steven D. Conradson,* P. Jeffrey Hay,
Richard L. Martin,* Marianne P. Wilkerson, Laura E. Wolfsberg

Los Alamos National Laboratory, Los Alamos, New Mexico 87545 (U.S.A.)
Received XXX, 2009

Submitted XXX; E-mail: *dlclark@lanl.gov*

Abstract: We describe the use of Cl K-edge X-ray Absorption Spectroscopy (XAS) and both ground state and time-dependent hybrid-Density Functional Theory (DFT) to probe electronic structure and determine the degree of orbital mixing in M-Cl bonds for $(C_5Me_5)_2MCl_2$ (M = Ti, **1**; Zr, **2**; Hf, **3**; Th, **4**; and U, **5**), where we can directly compare a class of structurally similar compounds for *d*- and *f*-elements. We report direct experimental evidence for covalency in M-Cl bonding, including actinides, and offer insight into the relative roles of the valence *f*- and *d*-orbitals in these systems. The Cl K-edge XAS data for the group IV transition metals, **1 – 3**, show slight decreases in covalency in M-Cl bonding with increasing principal quantum number, in the order Ti > Zr > Hf. The percent Cl $3p$ character per M-Cl bond was experimentally determined to be 25, 22, and 21% per M–Cl bond for **1-3**, respectively. For actinides, we find a shoulder on the white line for $(C_5Me_5)_2ThCl_2$, **4**, and distinct, but weak pre-edge features for $(C_5Me_5)_2UCl_2$, **5**. The percent Cl $3p$ character in Th-Cl bonds in **4** was determined to be 14 %,

with high uncertainty, while the U-Cl bonds in **5** contains 9 % Cl $3p$ character. The magnitudes of both of values are approximately half what was observed for the transition metal complexes in this class of bent metallocene dichlorides. Using the hybrid density functional theory (DFT) calculations as a guide to interpret the experimental Cl K-edge XAS, these experiments suggest that when evaluating An-Cl bonding, both $5f$- and $6d$-orbitals should be considered. For $(C_5Me_5)_2ThCl_2$, the calculations and XAS indicate that the $5f$- and $6d$-orbitals are nearly degenerate and heavily mixed. In contrast, the $5f$- and $6d$-orbitals in $(C_5Me_5)_2UCl_2$ are no longer degenerate, and fall in two distinct energy groupings. The $5f$-orbitals are lowest in energy and split into a 5-over-2 pattern with the high lying U $6d$-orbitals split in a 4-over-1 pattern, the latter of which is similar to the d-orbital splitting in group IV transition metal $(C_5R_5)_2MCl_2$ (R = H, Me) compounds. Time dependent-DFT (TD-DFT) was used to calculate the energies and intensities of Cl $1s$ transitions into empty metal based orbitals containing Cl $3p$ character, and provide simulated Cl K-edge XAS spectra for **1-4**. However, for **5**, which has two unpaired electrons, analogous information was obtained from transition dipole calculations. The simulations provide additional confidence in the interpretation of spectra based on ground state calculations. Overall, this study demonstrates that Cl K-edge XAS and DFT calculations represent powerful tools that can be used to experimentally evaluate electronic structure and covalency in actinide metal-ligand bonding. In addition, these results provide a framework that can be used in future studies to evaluate actinide covalency in compounds that contain transuranic elements.

Introduction

The transition elements have been broadly defined as those elements that have partially filled d– or f–shell orbitals in any of their commonly occurring oxidation states, and include the main transition or d–block elements, the lanthanide or $4f$–block elements, and the actinide or $5f$–block elements.[1] For d–block elements, the $3d$-, $4d$-, and $5d$–orbitals extend well into the periphery of the atom and can interact with ligand atoms to form covalent chemical bonds. In

contrast, the $4f$–orbitals of lanthanide elements are very core-like and their interactions with ligands are of little chemical consequence.[2] The actinide elements lie in between these two extremes, and there has been much debate over the ability of these elements to use either the $5f$– or $6d$–orbitals, or both, in chemical bonding interactions.[3-17]

In order to evaluate trends in metal and ligand orbital mixing as a function of $3d$-, $4d$-, $5d$-, and $6d/5f$-metal orbitals, we report on the analyses of transition metal and actinide bis-pentamethylcyclopentadienyl dichloride compounds $(C_5Me_5)_2MCl_2$ (M = Ti, **1**;[18] Zr, **2**;[19] Hf, **3**;[20] Th, **4**;[21,22] and U, **5**[21,22]). This series was carefully selected for study since it provides a unique family of structurally similar compounds with which to evaluate trends in metal and Cl orbital mixing down the series of $3d$-, $4d$-, $5d$-, and $6d/5f$-elements. The $C_5Me_5^{1-}$ system is important since the $C_5H_5^{1-}$ systems are not stable for actinide elements.[23,24] Moreover, since these bent metallocene dichlorides are among the most extensively utilized systems in organometallic research,[25-29] developing an understanding of covalency in their bonding is especially important and could have widespread impact.

Of the approaches to experimentally measure covalent metal-ligand bonding interactions,

M = Ti, Zr, Hf   M = Ti, Zr, Hf, Th, U, Np
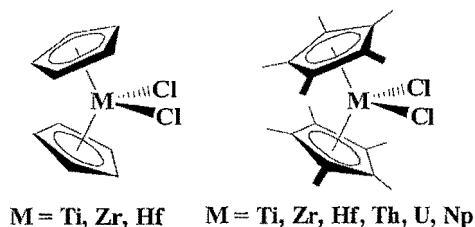
ligand K-edge X-ray Absorption Spectroscopy (XAS) has been established as a powerful technique to quantify ligand and metal orbital mixing in transition metal bioinorganic and inorganic compounds.[30-42] This technique probes bound state transitions that occur on the low energy side of the ligand K-edge, and involves excitation of ligand $1s$ electrons into molecular orbitals of primarily metal character[35] that also contain some ligand p character, due to covalent mixing. The intensity of the pre-edge transition is a direct measure of the ligand p orbital

contribution to the primarily metal-based antibonding orbital. Hence, ligand K-edge XAS provides a direct experimental measure of covalency in metal-ligand bonding.[35]

The goal of this contribution is to establish that Cl K-edge XAS in combination with modern density functional theory (DFT) simulations can be used to probe electronic structure, bonding, and covalency in light actinide (5f/6d) compounds for direct comparison with their 5d, 4d, and 3d counterparts. Given that **1 – 5** and $(C_5H_5)_2MCl_2$ (M = Ti, Zr, Hf, Th, and U; **6 – 10**, respectively) have been the center of recent theoretical[15,43-54] and experimental[36,40,55-58] studies, they are well suited for the Cl K-edge XAS and DFT experiments reported here, which provide a quantitative analysis of covalency in actinide bonding in comparison to analogous transition metal complexes.

Experimental Section

General Considerations. All compounds and samples were manipulated under helium or argon with rigorous exclusion of air and moisture by Schlenk, glovebox, and glovebag techniques. Toluene was distilled over sodium and benzophenone and degassed by three freeze-pump-thaw cycles. Polystyrene was acquired from PolySciences Inc. as 3.0 Micron Dry Form, exposed to vacuum (10^{-3} Torr) for 24 h before use, and verified to contain no chlorine by Cl K-edge XAS. The D_{2d}-Cs_2CuCl_4[59] intensity and energy calibration standard[32,35,60-63] was prepared as previously described. The $(C_5Me_5)_2MCl_2$ (M = Ti, **1**;[18] Zr,[19] **2**; and Hf,[20] **3**) compounds were obtained from Aldrich and crystallized from saturated solutions of hot toluene that were slowly cooled to -25 °C. The $(C_5Me_5)_2AnCl_2$ (An = Th,[21,22] **4**, and U,[21,22] **5**) compounds were synthesized as previously described and purified by crystallization from saturated solutions of hot toluene that were slowly cooled to -25 °C. Sample purity for all compounds was confirmed by ^1H NMR spectroscopy.[18-22]

XAS Sample Preparation. Samples were prepared by finely grinding the analyte (0.007 g) with polystyrene beads (0.120 g) to obtain a homogenous mixture that contained, by mass, 5.5 % analyte as described previously.[40] An aliquot of this mixture (0.010 g) was transferred to a vial

that contained polystyrene (0.070 g) and this new diluted mixture, which contained 0.69 %

analyte by mass, was ground with a mortar and pestle for 2 min to achieve small and finely

divided particles. An aliquot of this mixture (0.060 mg) was transferred to a vial and toluene

(400 μL) was added. The mixture was stirred with a glass stir rod until everything dissolved and

the solution was transferred into a 5 x 11 x 4 mm well that had been bored into an aluminum

block. The toluene was allowed to evaporate for 48 h under the helium atmosphere of the

glovebox, leaving a robust film fixed within the sample block. This approach is important for

two reasons. First, the polystyrene gives a suitable matrix for encapsulating radioactive

materials (Th, U), and the analytical procedure gives high reproduceability for sample

preparation, which has been shown to eliminate self-absorption effects in Cl XAS.

Chlorine K-edge XAS Measurements. The room temperature Cl XAS data were

recorded at the Stanford Synchrotron Radiation Laboratory (SSRL) and analyzed using the 54-

pole wiggler beamline 6-2 under ring conditions of 3.0 GeV and 85-100 mA in high magnetic

field mode of 0.9 Tesla with a Ni-coated harmonic rejection mirror and a fully tuned (3150 eV)

Si(111) double crystal monochromator. A chamber similar to that previously described was

used,[63] with the exception that two additional layers of radiological containment were introduced,

first with a beryllium window (50 μm thick) to separate the I_0 chamber from the beam pipe,

followed by a 4.5 μm polypropylene window to separate the I_0 and I_1 chambers. The sample

excitation fluorescence was measured under vacuum (10^{-7} Torr), and the Cl K-edge XAS was

collected against the incident beam using pairs of backward facing International Radiation

Detector XUV100 type photodiodes coated with 1000 Å of Al. The photodiodes were

closely spaced so that a 1-2 mm wide beam passed between them. Incident beam intensity was

measured as the scatter off of the He atmosphere with a photodiode pair in a front chamber.

Fluorescence from the sample was measured by an identically configured photodiode pair facing

the sample that was mounted at normal incidence to the oncoming beam that collected over a

wide solid angle because of its proximity 5-10 mm to the sample. The energy calibrations for the

Cl K-edge XAS were repeatedly conducted between sample scans, and based on the maximum

of the first pre-edge feature in the Cl K-edge XAS of D_{2d}-Cs$_2$CuCl$_4$,[32,35,60-63] at 2820.20 eV.

The Cl K-edge XAS data were collected with three different step sizes, which were 4.000, 0.072, and 3.899 eV for the pre-edge (2705 – 2801 eV), edge (2801 – 2835 eV), and post-edge (2835 – 3140 eV) regions, respectively. To obtain adequate statistics, 4 s counting times were employed and the spectra were collected twice. Different samples of crystalline **1 – 5** were examined during three different synchrotron runs to confirm reproducibility and establish error limits with the measurements. Error limits associated with the intensities for the resolved pre-edge features for **1 – 3** and **5** are 2%, while a larger margin of error, 10 %, is associated with the intensity of the poorly resolved pre-edge shoulder in the Cl K-edge XAS of **4**.

XAS Data Analysis. In typical data analysis for the Cl K-edge XAS, a first-order polynomial was fit to the pre-edge region (2780.0 – 2817.0 eV) and then subtracted from the experimental data to eliminate the background of the spectrum. As described previously, the data were normalized by fitting a first-order polynomial to the post-edge region of the spectrum (2830.0 – 3032.0 eV) and by setting the edge jump at 2835.0 eV to an intensity of 1.0.[36] Curve-fitting analyses were conducted using the program IGOR 6.0 with mathematical expressions employed by EDG_FIT,[64] and fits were performed over several energy ranges. The 1st and 2nd derivatives of each spectrum were used as guides to determine the number and positions of the spectral features for the curve-fitting analyses. Curve fits utilized pseudo-Voigt line shapes and a step function to model the pre-edge and rising edge spectral features.[35] For the pre-edge and white line features, a fixed 1:1 ratio of Lorentzian to Gaussian contributions were used, and for the step function, a 1:1 ratio of arctangent and error function contributions were employed.[35]

Electronic Structure Calculations. Electronic structure calculations were conducted on the (C$_5$Me$_5$)$_2$MCl$_2$, (M = Ti, Zr, Hf, Th, and U; **1 – 5**, respectively) and (C$_5$H$_5$)$_2$AnCl$_2$ (An = Th, **9**, and U, **10**) complexes using B3LYP hybrid density functional theory (DFT)[65] in the *Gaussian 03* code.[66] The Stuttgart 97 relativistic effective core potential and associated basis sets (minus the most diffuse function) were used for Ti, Zr, Hf, U, and Th. For the C and H atoms the 6-31G* basis sets were used, while for Cl the 6-31G* basis set was modified by re-contracting the *p*

functions to the B3LYP $2p$ through $6p$ atomic orbitals of Cl^{1-} (See Supporting Information). The re-contraction of the p space did not change the predicted structures and proved advantageous by providing a cleaner interpretation of the participating atomic orbitals in the molecular orbitals under consideration. These functionals and basis sets have been extensively tested for organometallic systems and shown to give good agreement with experimental data.[67-72] The populations of the Cl $3p$ orbitals of each compound were then obtained by Mulliken population analysis of each particular molecular orbital.

Simulated Cl K-edge Spectra. For $(C_5Me_5)_2MCl_2$ (M = Ti, Zr, Hf, and Th; **1 – 4**, respectively) and $(C_5H_5)_2ThCl_2$, **9**, Cl K-edge XAS were simulated using time dependent density functional theory (TD-DFT). This approach involves evaluating core electron excitations by exploiting the small amount of mixing of the core orbitals with the high lying unoccupied virtual orbitals. Specifically this analysis involves a <u>linear</u> response calculation, which enables the probability amplitudes to be extracted from the transition dipole moments between the calculated excited states and the ground states. The excitations originating from all of the intermediates states between the Cl 1s and the HOMO were not included so that only excitations from the core levels to virtual molecular orbitals could be analyzed. This allows the virtual orbitals to mix and reflect the presence of the core hole in chlorine. However, relaxations for other the occupied orbitals associated with the core hole were not included. Although excluding relaxations in the occupied orbitals associated with the core hole results in large errors associated with absolute calculated transition energies, this computation technique is capable of providing simulations that are in very good agreement with experimental measurements made on transition metal compounds. This was achieved by establishing a constant shift of 64.9 eV for all calculated spectra, to account for the omission of the atomic and extra-atomic relaxation associated with the core excitation, relativistic stabilization, and errors associated with the functional.[73]

Our first approximation to the DFT linear response methodology consisted in calculating transition dipoles among molecular orbitals. This approach was tested against TD-DFT by calculating the spectra of **1**, **2**, **3**, and **4** with both transition dipole and TD-DFT methodologies.

The spectra calculated from the MO transition dipoles are essentially identical to those from the TD-DFT calculations including the most salient features such as pre-edge features, relative intensity of peaks and the position of rising edge (see supporting information for the comparison). With this validation of the transition dipole method on closed-shell systems (**1 – 4**), we employed the transition dipole approach to simulate spectra for the open-shell $(C_5R_5)_2UCl_2$ (R = Me, **5**, and H, **10**) systems. The multiplet effects for uranium ($5f^2$) is expected to be small in this system because the two unpaired f-electrons are mostly localized on f-only orbitals resulting in little effect on the U-Cl bonding. A rigorous analysis for this open-shell system is underway which includes the four component relativistic effects, spin-orbital interactions, open-shell TD-DFT, and multiplet effects. All the calculated transition intensities were evenly broadened with a pseudo-Voigt function of half-width at half maximum of 0.33 eV and equal amounts of Gaussian and Lorentzian functions to emulate, as close as possible, the experimental spectrum.

Results and Discussion

The background subtracted, normalized chlorine K-edge XAS of the $(C_5Me_5)_2MCl_2$ (M = Ti, Zr, Hf, Th, and U; **1 – 5**, respectively) compounds are shown in Figure 1. Ligand K-edge
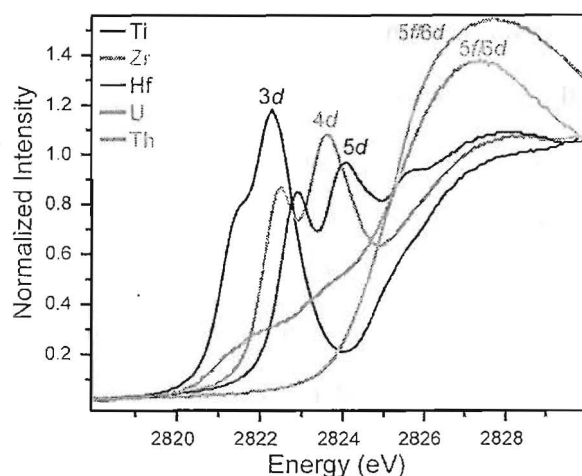

Figure 1. Experimental Cl K-edge X-ray absorption spectra for polystyrene encapsulated samples of $(C_5Me_5)_2MCl_2$ (M = Ti, black, Zr, brown; Hf, blue; Th, green; U, red; **1 – 5** respectively).

XAS of **1 – 5** were conducted on samples encapsulated in polystyrene matrices (0.7 % by mass of analyte). This represents a new approach to acquire high quality XAS data while minimizing X-ray self-absorption,[40] and simultaneously providing a layer of containment for radioactive materials by essentially fixing the analyte within the polystyrene. This also avoids the implementation of additional windows and chambers that can attenuate the incident beam and sample fluorescence.

Group IV Transition Metal Complexes. The Cl K-edge XAS for the transition metal $(C_5Me_5)_2MCl_2$ (M = Ti, **1**; Zr, **2**; and Hf, **3**) complexes are similar to the Cl K-edge XAS reported for the hydrogen substituted $(C_5H_5)_2MCl_2$ (M = Ti, Zr, and Hf; **6 – 8**, respectively) analogs, in that pre-edge features indicative of covalent M-Cl interactions are apparent between 2821 – 2824 eV, Figure 1 and Table 1.[36,40] For these compounds, the energy position of the pre-edge peaks are not largely affected by the identity of the ancillary ligand, i.e. $(C_5Me_5)^{1-}$ vs. $(C_5H_5)^{1-}$, Table 1. However, significant energy shifts occur when changing the metal ion from $3d$ to $4d$ to $5d$. For example, the pre-edge peaks at 2822.41 and 2823.62 eV for $(C_5Me_5)_2ZrCl_2$ are resolved from the rising edge and at lower energy than the analogous features observed for $(C_5Me_5)_2HfCl_2$, at 2822.86 and 2823.93 eV, Table 1. This is consistent with trends observed for the $(C_5H_5)_2MCl_2$ complexes, which demonstrated that as the principal quantum number is increased, the pre-edge energy decreases,[40] such that Ti < Zr < Hf, which reflects the expected rise in energy for the $3d$-, $4d$-, and $5d$-orbital final states.

Although the pre-edge features in the Cl K-edge XAS for **1 – 3** are well separated from the white lines, the close proximities of **2** and **3** to the rising edges complicates rigorous determination the inflection points for the white lines, Figure 1. The spectra for **1 – 3** also contains a shoulder on the rising edge that further clouds identifying the inflection point, which is more pronounced in the $(C_5Me_5)_2HfCl_2$ case than for $(C_5Me_5)_2TiCl_2$. Extrapolation of the rising edge, near 2826 eV, to the base line suggests that the energy of the white line is highest for **1**, intermediate for **2**, and lowest for **3**. This implies deeper binding energies for the Cl $1s$ orbitals in

1 and implies that the covalency of the M-Cl bond changes in the order Ti-Cl > Zr-Cl > Hf-Cl.[32,35] The relative intensities of the pre-edge features for $(C_5Me_5)_2MCl_2$ (1 – 3) are consistent with this qualitative edge analysis, Figure 1.

The spectral features of 1 - 3 were modeled using pseudo-Voigt line shapes with a fixed 1:1 Lorentzian to Gaussian ratio, Figure 2.[35] For $(C_5Me_5)_2MCl_2$, 1 and 2 (Ti, Zr), the curve-fitting analysis and the 1st and 2nd derivatives of the data reveal that the pre-edge features are well modeled by two functions. Another gauge that can be used to assess the curve-fitting model relies on evaluating the shapes of residual peaks, which are obtained by subtracting from the data the functions used to generate the fit, with the exception of the function used to model the peak of interest. For 1 and 2, the residual peaks (Supplemental data) are symmetric and similar in shape to the corresponding pseudo-Voigt functions. This indicates a good fit and suggests that the two pre-edge features can be resolved with confidence. This type of analysis is common for evaluating curve-fitting in EXAFS,[72,74,75] and we find it to be extremely useful in evaluating XAS for covalency studies.

The Cl K-edge XAS of $(C_5Me_5)_2HfCl_2$, 3, provides an example where employing residual data and residual peak shape analysis provided unique insight. For example, fitting the pre-edge region of the Cl K-edge spectrum of 3 with two pre-edge features in analogy to $(C_5Me_5)_2ZrCl_2$, 2, and $(C_5H_5)_2MCl_2$ (M = Ti, Zr, Hf; 6 – 8, respectively) provided an adequate model with good correlation coefficients. However, the residual data deviated significantly from zero near 2824 eV, and the residual pre- and post-edge peaks were highly asymmetric. This prompted closer analysis of the 1st and 2nd derivatives (see Supplemental Data) which suggested that a third feature had been missed and should be considered for analysis of the Cl K-edge XAS of 3, Figure 2. Including this third pre-edge feature in the curve-fit did improve the correlation coefficient. Moreover, with three features, the residual data does not appreciably deviate from zero and the three resulting highly symmetric pre- and post-edge residual peaks were similar in shape to the pseudo-Voigt functions used to generate the fit. The presence of this third feature
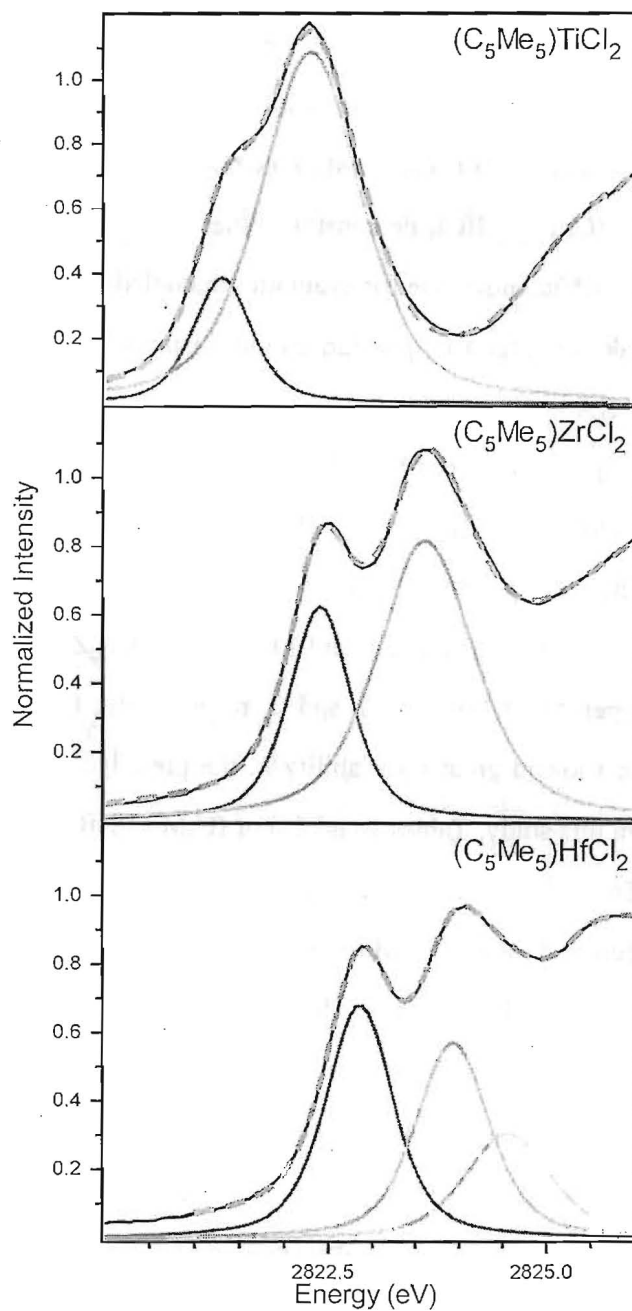
Figure 2. Cl K-edge X-ray absorption spectra (black), curve fits (red dashes), and pre-edge pseudo-Voigt peaks used to generate the fit (blue, orange, and green lines) for polystyrene film samples of $(C_5Me_5)_2MCl_2$ (M = Ti, top, Zr, center; Hf, bottom, **1**, **2** and **3** respectively).

does not appreciably affect the peak positions of the first two features or the total pre-edge peak intensities. It does, however, represent a significant difference between the electronic structure model of $(C_5Me_5)_2HfCl_2$ relative to **1** and **2** and to the $(C_5H_5)_2MCl_2$ analogues, vide infra. Hence, the Cl K-edge XAS of $(C_5Me_5)_2HfCl_2$ demonstrates the limitations associated with relying too heavily on correlation coefficients alone for evaluating modeled data, and suggests that residual data and residual peak analysis can provide useful insights and additional confidence for interpreting Cl K-edge XAS.

The percent Cl $3p$ character per M-Cl bond was determined for **1 – 3** using the pre-edge intensities for the pseudo-Voigt functions and the D_{2d}-Cs_2CuCl_4 intensity standard, defined as having 7.5 % Cl $3p$ character per Cu-Cl bond,[32,35,60-63] Table 1. The two pre-edge intensities of 0.30 and 1.48 for $(C_5Me_5)_2TiCl_2$, **1**, and 0.51 and 1.08 for $(C_5Me_5)_2ZrCl_2$, **2**, correspond to 25 and 23% Cl $3p$ character per M-Cl bond for **1** and **2**, respectively. For compound **1** attempts to reproduce its spectrum showed greater variability in the pre-edge intensities for **1** than for the compounds analyzed in this study, Tables 1 and 2. For $(C_5Me_5)_2HfCl_2$, **3**, the three pre-edge peak intensities of 0.62, 0.56, and 0.35 and correspond to 22% Cl $3p$ character for each Hf-Cl bond. Despite the greater electron donating $(C_5Me_5)^{1-}$ ligand, these values are remarkably similar to the total % Cl $3p$ character recently determined by Cl K-edge XAS for the hydrogen substituted $(C_5H_5)_2MCl_2$ analogues, **6 - 8**,[40] which demonstrated that as the principal quantum number is increased in group IV transition metal metallocenes,[40] the covalency of the M-Cl bond decreases, such that Ti > Zr > Hf, Table 2.

Cl K-edge Spectra of Actinide Complexes. The Cl K-edge XAS for $(C_5Me_5)_2ThCl_2$, **4**, and $(C_5Me_5)_2UCl_2$, **5**, both contain pre-edge features indicative of An-Cl covalency. For **4**, the pre-edge region differs from that of the transition metal analogues, in that it contains only a single pre-edge shoulder at 2825.58 eV. This shoulder was modeled using pseudo-Voigt line shapes with a fixed 1:1 Lorentzian to Gaussian ratio, and the correlation coefficient, the residual data, and residual peak shape indicate a high quality curve-fit, Figure 3. Since the pre-edge

appears as a weak shoulder on the white line (Table 1), the intensity of 1.02 has a high degree of uncertainty, complicating the quantitative comparison with the other compounds in the series.

In contrast to $(C_5Me_5)_2ThCl_2$, **4**, the Cl K-edge XAS for $(C_5Me_5)_2UCl_2$, **5**, contains three clear pre-edge features that can be resolved from the rising edge. These features were also modeled using pseudo-Voigt line shapes with a fixed 1:1 Lorentzian to Gaussian ratio, Figure 3.
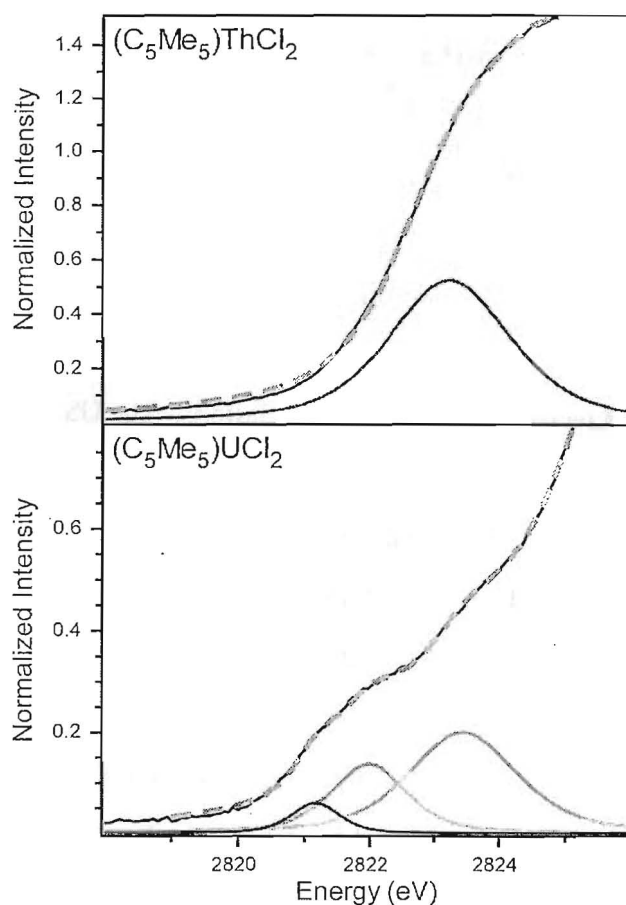
Figure 3. The Cl K-edge X-ray absorption spectra (black line), curve fits (red dashes), and pre-edge pseudo-Voigt peaks used to generate the fits (blue, orange, and green lines) for polystyrene film samples of $(C_5Me_5)_2MCl_2$ (M = Th, top; U, bottom, **4** and **5** respectively).

Two of the features are significantly low in energy, at 2821.17, 2821.99 eV, and one is at 2823.44 eV, which is higher in energy than the first pre-edge feature observed for the transition

13

metal analogs, **1 - 3**, and **6 - 8**.[36,40] The correlation coefficients, the residual data, and residual peak shapes suggest that the curve-fitting analysis provides a good model for the experimental data. Using the in intensities of the pre-edge pseudo-Voigt functions, which are 0.05, 0.19, and 0.40, and the D_{2d}-Cs_2CuCl_4 intensity standard,[32,35,60-63] the % Cl $3p$ character per U-Cl bond was quantitatively determined to be 9% for **5**, and the magnitude of this value is approximately half what was observed in the analogous group IV transition metal counterparts, Tables 1 and 2. This result is significant given that covalency in $5f$-element chemistry has been highly debated for decades.[3-17] The Cl K-edge XAS of **5** shows direct experimental evidence for covalency in actinide metal-bonding, and provides a quantitative experimental method for evaluating the degree of orbital mixing between Cl and U in the U-Cl bonds. For peak assignments, and assessing the relative roles of $5f$- versus $6d$-orbitals in bonding, we turn to electronic structure calculations as a guide.

Ground State Electronic Structure Calculations. The GS-DFT calculations performed on $(C_5Me_5)_2MCl_2$ (M = Ti, **1**; Zr, **2**; and Hf, **3**) indicate that the electronic structure of **1 - 3** are quite similar to their $(C_5H_5)_2MCl_2$ analogues, Table 3.[36,40,54] The calculations show that the HOMO, and the subsequent three lower lying orbitals, have predominantly (C_5Me_5) character with small contribution from the M-Cl bonds. These occupied orbitals are approximately 1 eV higher in energy than a block of six primarily Cl $3p$ orbitals that span only ~1.2 eV. For **1 - 3**, the first five unoccupied orbitals have predominantly metal nd character with a calculated HOMO/LUMO gap of 3.58, 4.22 and 4.51 eV for **1**, **2**, and **3** respectively. For all three transition metal $(C_5Me_5)_2MCl_2$ complexes, the LUMO has $1a_1$ symmetry, and is best described as M-Cl π-antibonding. This oribital is significantly lower in energy than a higher lying set of four primarily metal nd molecular orbitals ($1b_2$, $1b_1$, $1a_2$, and $2a_1$), which are M-Cl σ-, π-, π-, and σ-antibonding, respectively. For Ti and Zr (**1**, **2**), these four nd-orbitals span only $ca.$ 0.9 eV, Figure 4, resulting in a 4-over-1 d-orbital splitting pattern similar to that reported for $(C_5H_5)_2MCl_2$ (M = Ti, Zr, and Hf).[36,40,54] In constrast, the d-orbital splitting pattern for $(C_5Me_5)_2HfCl_2$, **3**, differs from **1** and **2** in that there is a low lying orbital of $1a_1$ symmetry, an

14

intermediate $1b_2$ orbital, and a manifold of three higher lying orbitals of $1b_1$, $1a_2$, and $2a_1$ symmetries, giving a 3-over-1-over-1 d-orbital spitting pattern, Figure 4. It has been shown previously that all five nd-orbitals are necessary to understand the XAS intensities due to a combination of σ and π orbital interactions with the Cl levels at lower energy.[36,40,54] The resulting d-orbital splitting pattern will be important for the interpretation of the XAS spectrum of **3**.

The DFT calculations conducted on the optimized structures of $(C_5R_5)_2AnCl_2$ (An = Th and U; R = H and Me) shows that the electronic structure model of the actinide complexes contains many similarities to their transition metal analogues. The calculations conducted on $(C_5R_5)_2UCl_2$ (R = Me, **5**, and H, **10**) converged normally to the triplet ground state with two unpaired predominantly $5f$ electrons. For the occupied orbitals, these results are similar to the closed-shell Xα-SW molecular orbital calculations previously reported for $(C_5H_5)_2UCl_2$,[45] **10**, in that both analyses show four occupied predominantly cyclopentadienyl orbitals above six occupied orbitals that have mainly Cl $3p$ character. In this sense, these calculations are also similar to what was observed in **1 – 3** and **6 – 9**.[36,40,54] As opposed to the closed-shell Xα-SW calculations,[45] which forced the highest lying two $5f$ electrons to be spin paired, our open-shell triplet calculations for **10** show that the two highest lying and singly occupied molecular orbitals (SOMOs) have predominantly $5f$ character, and are close in energy to other occupied cyclopentadienyl orbitals. For $(C_5Me_5)_2UCl_2$, **5**, the highest two alpha spin orbitals are mainly (C_5Me_5) based. Since these two orbitals have matches found in the beta-spin orbitals they do not represent unpaired spin density. The orbitals containing the unpaired spin lie lower in energy, and are again dominated by U $5f$ character. This is confirmed by a natural orbital analysis, which generates two largely U $5f$-orbitals with occupation numbers close to 1. For both **5** and **10**, there are approximately 3 eV differences between the occupied and five unoccupied $5f$-orbitals, which span only 0.76 and 0.80 eV for $(C_5H_5)_2UCl_2$ and $(C_5Me_5)_2UCl_2$, respectively, Figure 4 and Table 4. However, caution must be exercised when interpreting these ground state DFT orbital energies for open-shell systems to explain the peak splitting observed in experiments without including spin-orbit interactions and multiplet effects.
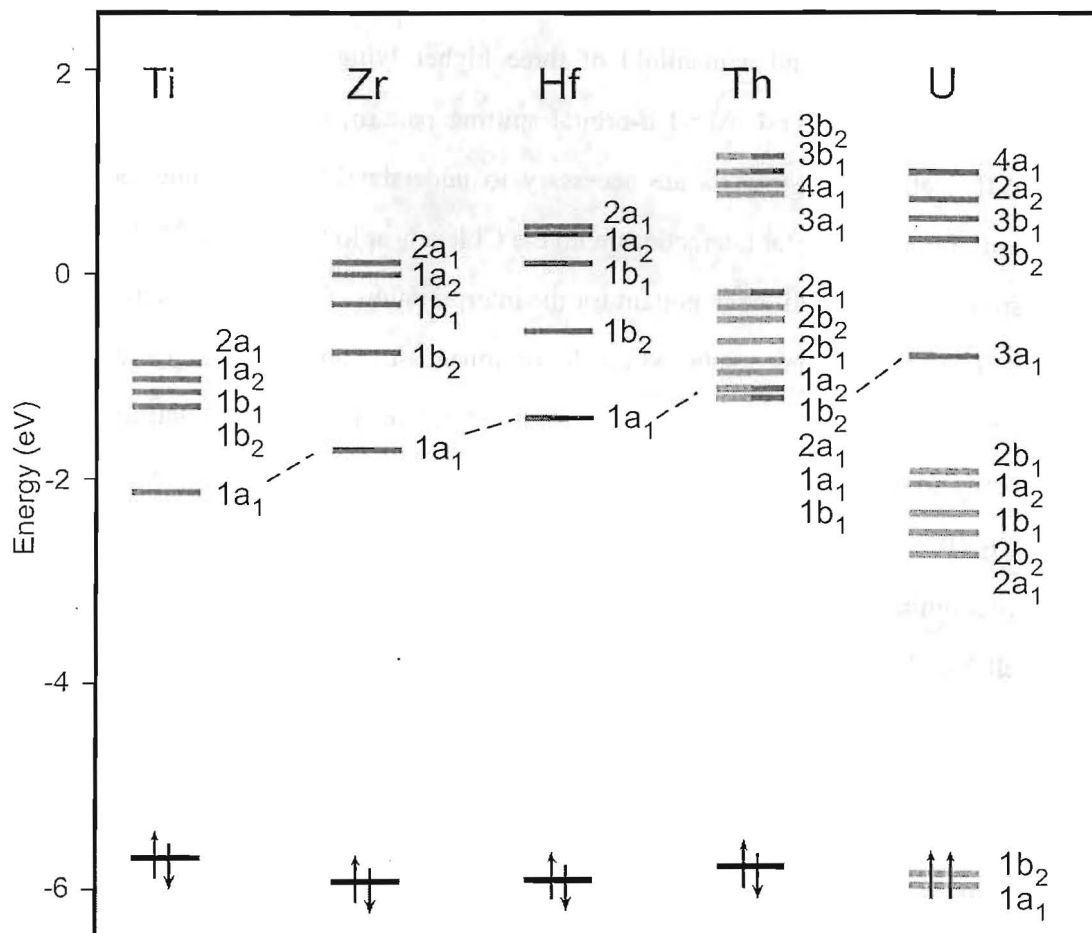
Figure 4. Calculated molecular orbital energy diagram for $(C_5Me_5)_2MCl_2$ (M = Ti, **1**; Zr, **2**; Hf, **3**; Th,[a] **4**; and U[a] **5**) showing orbitals that have primarily nd character (blue), primarily $5f$ (red), and orbitals with >10% nd and >20 $5f$ character are shown as half red and blue.

[a]Although orbital symmetry labels associated with the C_{2v} point group are used to simplify the electronic structure description for $(C_5Me_5)_2MCl_2$ compounds, the optimized structures deviate from pure C_{2v} symmetry.

For $(C_5Me_5)_2UCl_2$, **5**, and $(C_5H_5)_2UCl_2$, **10**, we find the well-known 4-over-1 splitting pattern for the virtual $6d$-orbitals, as shown for **5** in Figure 4 with C_{2v} symmetry labels used for comparison with the transition metal analogs, although the actual symmetry used in the $(C_5Me_5)_2UCl_2$ calculation was C_l. Superimposed on this picture is the addition of the $5f$-orbital

16

manifold, which has a combination of non-bonding, σ- and π-antibonding interaction with the Cl lone pairs. For **5**, steric repulsion between the $C_5Me_5^{1-}$ rings gave an optimized geometry with no symmetry, which complicates the bonding comparison to the transition metal analogs. To facilitate this comparison, rather than forcing the geometry of **5** to be rigorous C_{2v} symmetric, which decreases (C_5Me_5 ring centroid)-U-(C_5Me_5 ring centroid) angle and can have significant electronic affects,[44] two calculations were performed on the $(C_5H_5)_2UCl_2$, **10**, analog. The first calculation on **10** was conducted in rigorous C_{2v} symmetry, and the second with the geometry optimized, which results in C_I symmetry. Both of these calculations, qualitatively, provide a similar bonding descriptions to the what was observed for $(C_5Me_5)_2UCl_2$, Table 4, and the calculated Kohn-Sham orbitals for **10** in C_{2v} symmetry are shown in Figure 5. From the figure it

| 2a$_1$ | 2b$_2$ | 1b$_1$ | 1a$_2$ | 2b$_1$ |
| (70) | (71) | (72) | (73) | (74) |

| 1a$_1$ | 1b$_2$ |
| (68) | (69) |
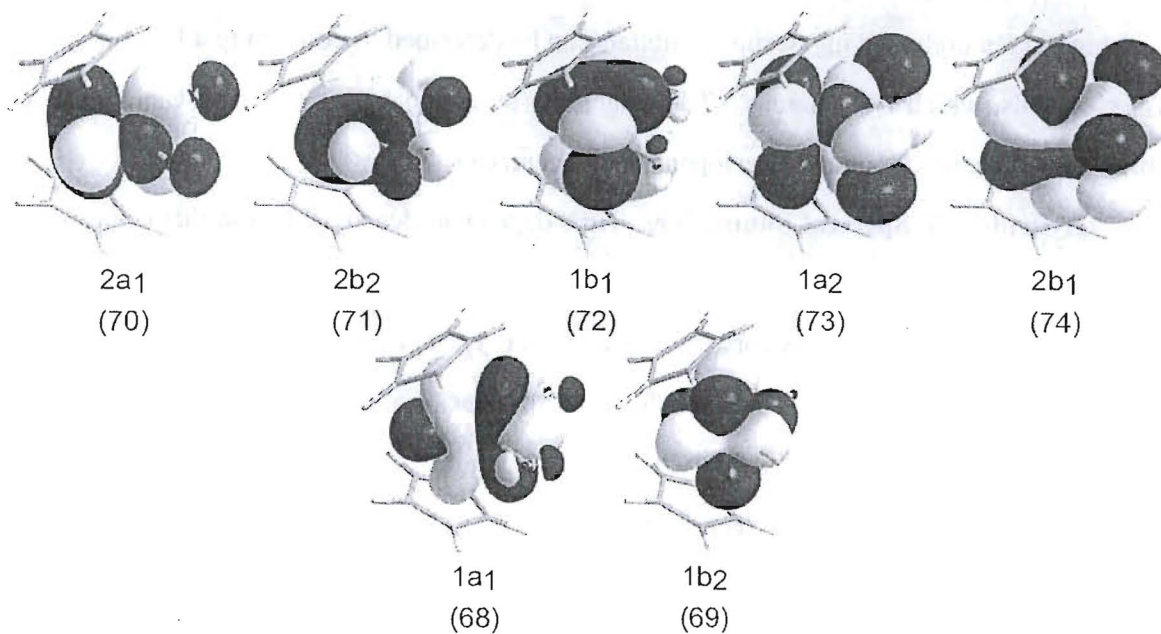
Figure 5. The relevant Kohn-Sham orbitals that have primarily 5*f* character for C_{2v}-$(C_5H_5)_2UCl_2$. Only the U 5*f* and and Cl 3*p* contributions are shown.

is easy to see the nature of U-Cl σ- or π-antibonding interactions. The $1b_1$ and $1b_2$ orbitals are essentially non-interacting 5*f*-orbitals. The $1a_1$ and $2b_2$ orbitals represent U-Cl π-antibonding interactions that are within the UCl_2 plane, while the $1a_2$ and $2b_1$ orbitals represent U-Cl π-

antibonding interactions that are perpendicular to the UCl_2 plane. The $2a_1$ oribital is U-Cl σ-antibonding. There is no real reason for the pronounced 5-over-2 pattern of $5f$-orbital energies, and the stabilization of the $1a_1$ and $1b_2$ $5f$-orbitals seen in Figure **4** is likely an artifact of those orbitals being singly occupied in the calculation.

For $(C_5Me_5)_2ThCl_2$, **4**, and $(C_5H_5)_2ThCl_2$, **9**, the situation is more complicated due to the near degeneracy of the $5f$- and $6d$-orbitals and strong $5f$-$6d$ hybridization.[49] All twelve of the unoccupied metal based orbitals contain both $5f$ and $6d$ character and split into two groups: eight and four. The lower eight Th-Cl antibonding orbitals, which span only 1.1 and 1.4 eV for $(C_5H_5)_2ThCl_2$ and $(C_5Me_5)_2ThCl_2$, respectively, Figure 4 and Table 4, correspond to the single pre-edge shoulder in XAS spectra. The electronic structure model for occupied orbitals of **4** and **9**, which are closed shell systems, are similar to what was observed for the d^0 metallocenes, **1** – **3**, in that the ten highest lying occupied orbitals can be described as containing a low lying block of six orbitals, which have mainly Cl $3p$ character, separated by >1 eV from a block of four orbitals that have predominantly cyclopentadienyl character.

Hybrid-DFT Spectral Simulations. Time dependent density function theory (TD-DFT) has been recently applied to simulate Cl K-edge XAS for d-block metallocenes.[36,40,54] The TD-DFT simulated Cl K-edge XAS for $(C_5Me_5)_2MCl_2$ (Ti, **1**; Zr, **2**; and Hf, **3**) agree well with the experimental data and show two pre-edge features for **1** and **2**, and three features for **3**, Figure 6. Compared to previous reports for the $(C_5H_5)_2MCl_2$ compounds, where M is Ti, Zr, and Hf, the calculations show that the more electron donating $(C_5Me_5)^{1-}$ ligand increases the energy of the pre-edge features and decreases the covalency of M-Cl bond, though the overall pre-edge features are very similar between $(C_5H_5)^{1-}$ and $(C_5Me_5)^{1-}$ containing complexes. For example, as observed in the spectra for $(C_5H_5)_2MCl_2$, the first pre-edge feature in the Cl K-edge XAS of **1** – **3** are attributed to an electronic excitation from the Cl $1s$ orbital into a M-Cl π-antibonding orbital that has a_1 symmetry, Figure 7. The second pre-edge feature of **1** and **2** (Ti, Zr) is attributed to an electronic excitation from the Cl $1s$ orbital into the manifold of higher lying M-Cl σ- and π-antibonding orbitals of $1b_2$, $1b_1$, $1a_1$ and $2a_1$ symmetries. Since these four orbitals are very close
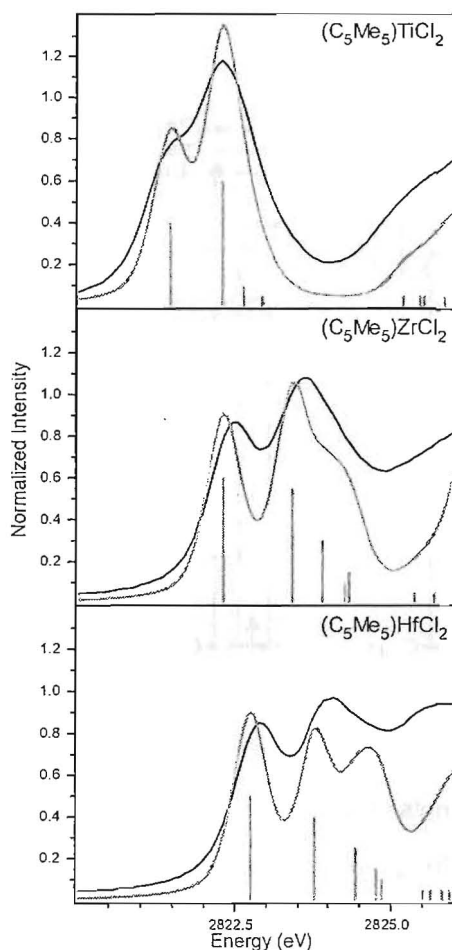
Figure 6. The Cl K-edge X-ray absorption spectra (black), the TD-DFT calculated spectrum (red), and calculated transitions (red bars) for polystyrene films of $(C_5Me_5)_2MCl_2$ (M = Ti, **1**, Zr, **2** and Hf, **3**). The height of the black bars represents the calculated oscillator strength for the individual transitions.

in energy, individual transitions could not experimentally be resolved. This assignment is essentially identical to that previously reported for the $(C_5H_5)_2MCl_2$ analog spectra of **6 – 8** (Ti, Zr, Hf). The Cl K-edge XAS of $(C_5Me_5)_2HfCl_2$, **3**, Figure 2, is unique among the $(C_5H_5)_2MCl_2^{36,40,54}$ and $(C_5Me_5)_2MCl_2$ compounds, in that electronic excitations from the Cl $1s$ orbital to the Hf-Cl σ-antibonding $1b_2$ orbital, can be resolved from transitions to the three remaining higher lying d- orbitals. Hence, the second pre-edge feature in the Cl K-edge XAS of
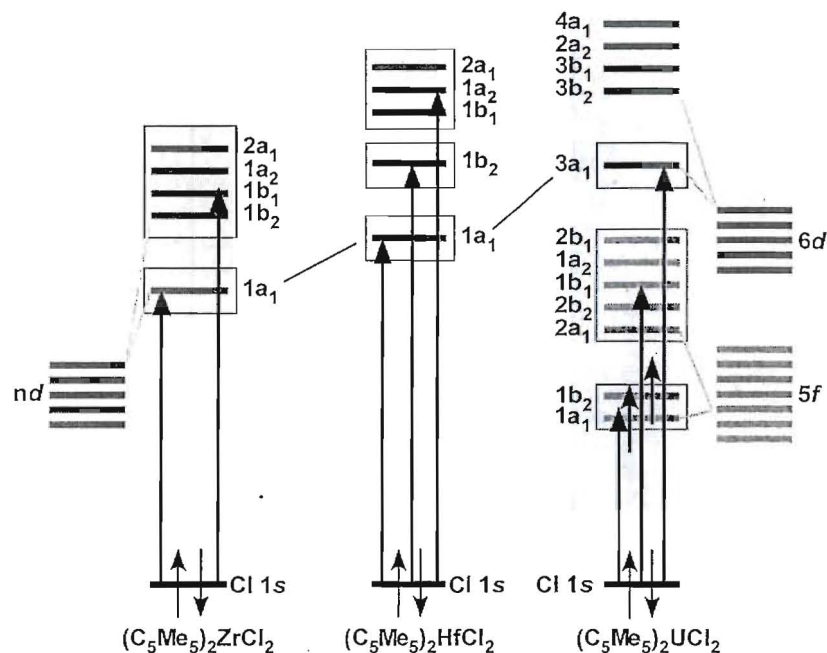
Figure 7. A qualitative molecular orbital scheme that compares the interpretation of the pre-edge transitions for $(C_5Me_5)_2ZrCl_2$ (*left*), $(C_5Me_5)_2HfCl_2$ (*middle*), and $(C_5Me_5)_2UCl_2$ (*right*) (**2**, **3**, and **5**, respectively).

3 is attributed to a Cl $1s \rightarrow 1b_2$ transition, and the third pre-edge feature stems from an electronic excitation from the Cl $1s$ orbital to the σ- and π-antibonding orbitals of $1b_1$, $1a_1$ and $2a_1$ symmetries, Figure 7.

The simulated spectra for **1 – 3** are in excellent agreement with the experimental spectra with the 4-over-1 and 3-over-1-over-1 d-orbital splitting patterns predicted by the GS-DFT calculations for $(C_5Me_5)_2MCl_2$ (Ti, Zr, Hf), respectively, Figure 4. In addition, the experimental Cl K-edge XAS provides validation for the d-orbital splitting in a quantitative manner, as predicted by molecular orbital calculations. For example, for **2** the 1.21 eV peak splitting in the experimental Cl K-edge XAS is similar to the theoretical predication of 1.1 eV. For **3**, the three peaks are separated by 1.07 and 0.63 eV, which is close to the 1.1 and 0.6 eV prediction.

The calculated Cl K-edge X-ray absorption spectrum of $(C_5Me_5)_2ThCl_2$, **4**, shows only one pre-edge feature corresponding to transitions to the lower group of nearly degenerate and heavily mixed $5f$- and $6d$-orbitals, Figure 8. This prediction is consistent with experimental

Figure 8. (**Top**) The experimental Cl K-edge X-ray absorption spectrum for $(C_5Me_5)_2ThCl_2$, **4**, (black) is compared to the simulated TD-DFT spectrum (red). (**Bottom**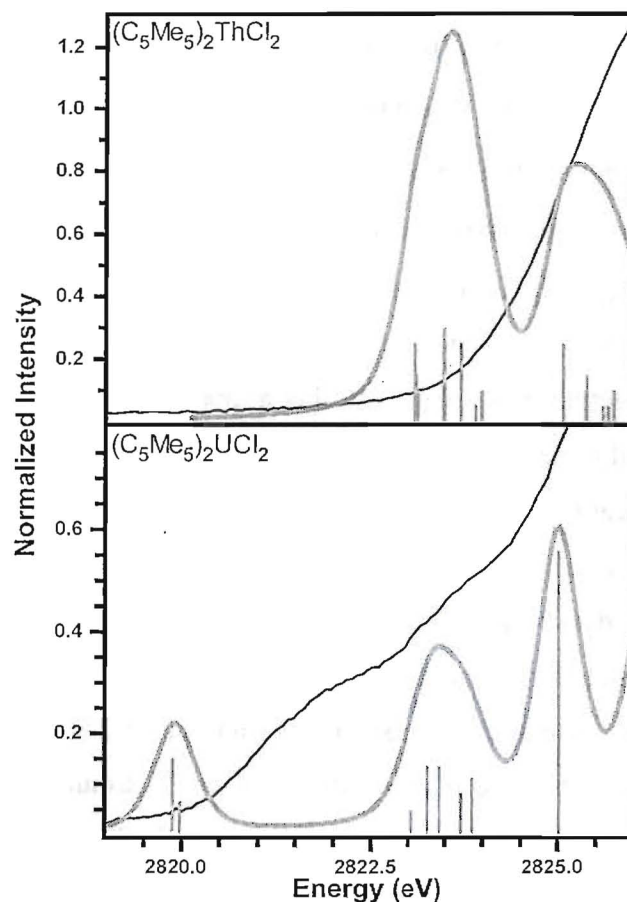) The experimental Cl K-edge X-ray absorption spectrum for $(C_5Me_5)_2UCl_2$, **5**, (black) is compared to the simulated dipole transition spectrum (red). In both comparisons, the calculated transitions are indicated below the spectrum as red bars whose height represents the calculated oscillator strength for the individual transitions.

spectra containing a single pre-edge feature that is close in energy to the white line. These results indicate that the pre-edge shoulder in the experimental Cl K-edge XAS of **4** is attributed to Cl $1s$-electron excitations into the manifold of eight metal based $5f/6d$ Th-Cl antibonding orbitals. We point it out that the calculated energy of this pre-edge feature does not match the experimental data as well as was observed for the transition metal $(C_5Me_5)_2MCl_2$ compounds. This suggests that the constant shift of 64.9 eV applied for actinide systems, which was applied to all calculated spectra and appropriate for transition metal complexes, may not sufficiently account for the omission of the atomic and extra-atomic relaxation associated with the core excitation, relativistic stabilization, and errors associated with the functional in actinide systems.[73]

Due to the open-shell ground state of $(C_5Me_5)_2UCl_2$, **5**, which contains two unpaired electrons, the XAS spectrum was simulated using a dipole transition calculation as opposed to TD–DFT. As discussed in the experimental section, TD–DFT and dipole transition calculations gave essentially identical results for the closed-shell systems, **1 – 4**. For **5**, the dipole transition simulated spectrum is in good agreement with the experimental data as shown in Figure **8**. For example, both calculated and experimental spectra show three pre-edge features. The first feature is attributed to a Cl $1s$ electron excitation into the SOMO-1 and SOMO, Figures **4** and **8**. The second feature is attributed to electronic excitations from the Cl $1s$ orbital into a manifold of five higher lying $5f$-orbitals, while the third feature involves electronic excitations into a U-Cl π-antibonding orbital, which has a_1 symmetry and primarily $6d$ character. These data suggest that the spectrum of $(C_5Me_5)_2UCl_2$ differs from those of **1 – 4**, in that the spectrum of **5** contains distinct $5f$ and $6d$ components. Comparing the Cl K-edge XAS for $(C_5Me_5)_2MCl_2$ with M = Ti, Zr, Hf, and U provides confidence in these assignments since it shows that descending the periodic table results in energy increases for the $1s \rightarrow a_1$ transitions, which are 2821.31, 2822.41, 2822.86, and 2823.44 eV, respectively, and are consistent with the expected energies of the $3d$, $4d$, $5d$, and $6d$ final orbital states, Figures 4 and 8. Since DFT-calculations predicted transitions involving other higher lying $6d$-orbitals to be high in energy, close to the white line, and most likely could not be experimentally resolved, their contribution to covalency in the U-Cl bond is neglected in the following discussions.

The experimental Cl K-edge XAS provides valuable validation for the electronic structure analysis of $(C_5Me_5)_2UCl_2$, **5**, by showing three pre-edge features. However, theoretical calculations over-estimate the peak splittings. The calcualted SOMO-LUMO energy gap is 3.13 eV while only 0.82 eV was observed experimentally. The experimentally determined 1.45 eV $5f/6d$-orbital energy gap is slightly larger than the calculation suggests, which is 1.12 eV. By carrying out the ground-state DFT calculation without spin-orbit and multiplet effects, it is not surprising to have this difference, and a thorough theoretical investigation on these effects is underway. Overall, the DFT calculations are in agreement with the experimental Cl K-edge XAS of $(C_5Me_5)_2UCl_2$, especially in predicting that the $5f$-orbitals in **5** are split in a 5-over-2 pattern and that the higher lying $6d$-orbitals split in a 4-over-1 pattern.

Comparing the experimental and simulated Cl K-edge XAS of $(C_5Me_5)_2MCl_2$ (M = Ti, Zr, Hf, Th and U; **1** - **5**, respectively) offers unique opportunity to evaluate the relative roles of the valence f- and d-orbitals in bonding. For example, comparing **4** and **5** provides insight into how electronic structure varies as the actinide series is traversed from left to right. In this case, transitions involving molecular orbitals that contain $5f$ character are lower in energy for $(C_5Me_5)_2UCl_2$ than for $(C_5Me_5)_2ThCl_2$, which is consistent with the previously reported Xα-SW molecular orbital calculations performed on $(C_5H_5)_3M$ (M = U, Np, Pu, Am, Cm, Bk, Cf)[76] and $(C_8H_8)_2M$ (M = Th, Pa, U, Np, and Pu).[77] The relative mixing of the metal and chlorine orbitals can also be evaluated as a function of increasing principal quantum number by comparing the intensities of the pre-edge features in the Cl K-edge XAS for **1** – **3**, and **5**, which are directly related to the percentage of Cl $3p$ character per M-Cl bond.[35] Both the calculated and experimental results indicate that the percentage of Cl $3p$ character per M-Cl bond follows the trend **1** > **2** > **3**. However, these data suggest that the difference is small in magnitude, similar to observations made on the $(C_5H_5)_2MCl_2$ analogues.[40] For example, the calculated % Cl $3p$ character for **1**, **2**, and **3** are 16, 14 and 12 %, while the experimentally determined values are 25, 23 and 22 %, respectively, Table 2. For $(C_5Me_5)_2UCl_2$, **5**, the Mulliken population analysis of 9 % Cl $3p$ character per U-Cl bond, which excludes contributions from the four highest lying $6d$-orbitals since transitions involving these orbitals were not experimentally resolved, is in

excellent agreement with the experimental result of 12 %, Table 2. Both the theory and experiment show that the U $5f$-orbitals are involved in covalent bonding to form antiboning orbitals, which were experimentally determined to contain a total of 4 % Cl $3p$-character. Moreover, these data also indicate that the U $6d$-orbitals are involved, and provide the opportunity to evaluate the $6d$ vs. $5f$ contributions to covalency. Hence for **5,** the experimental data suggests that the antibonding molecular orbital of $3a_1$ symmetry, which is primarily a U $6d$-orbital, contains 6 % Cl $3p$ character. This value is similar in magnitude and slightly larger than the total orbital mixing between the U $5f$- and Cl $3p$-orbitals. In addition, the % Cl $3p$ character in the $3a_1$ orbital in **5** is also similar to what was observed in the analogous molecular orbitals of $1a_1$ symmetry of the d-block metallocenes, but slightly less than the 9 % Cl $3p$ character associated with $(C_5Me_5)_2HfCl_2$. Overall, these covalency trends are similar to the trends revealed by previously reported measurements that used gas-phase photoelectron spectroscopy to probe the occupied orbitals of metallocene complexes.[56-58]

Concluding Remarks

In summary, ground state and hybrid-DFT calculations were used in conjunction with Cl K-edge XAS to evaluate trends in metal and ligand orbital mixing as a function of $3d$, $4d$, $5d$, and $6d/5f$ metal orbitals in a series of structurally similar $(C_5Me_5)_2MCl_2$ (M = Ti, Zr, Hf, Th, and U; **1 − 5,** respectively) complexes. For the Ti, Zr, and Hf containing compounds, the interpretation of the experimental and theoretical data are quite similar to the $(C_5H_5)_2MCl_2$ (M = Ti, Zr, and Hf; **6 − 8,** respectively)[36,40,54] analogues, in that the % Cl $3p$ character in the M-Cl bonding decreases as group IV is descended. These results also indicate that for group IV metallocene, all five metal-based orbitals ($1a_1$, $1b_2$, $1b_1$, $1a_2$, and $2a_1$) should be considered when evaluating M-Cl bonding, and show that for **1** and **2** the d-oribitals split in a 4-over-1 pattern, which is similar to previous reports on **6 − 8.**[36,40,54] For $(C_5Me_5)_2HfCl_2$, **3,** a similar trend is observed with the exception that there is a large energy separation between the transitions involving the $1b_2$ and $1b_1$ orbitals. Hence for **3,** the theoretical and experimental analyses suggests that the d-orbitals are split in a 3-over-1-over-1 pattern.

The analyses of **1 – 3** provide a basis to evaluated $(C_5Me_5)_2AnCl_2$ compounds, and surprisingly pre-edge features indicative of covalency were also present in the Cl K-edge XAS for $(C_5Me_5)_2ThCl_2$, **4**, and $(C_5Me_5)_2UCl_2$, **5**. The Cl K-edge XAS of **4** and **5** are significantly different than the group IV transition metal analogues, and these results indicate that both 5*f*- and 6*d*-orbitals should be considered when evaluating An-Cl bonding. For **4**, the 5*f*-orbitals involved in the Th-Cl bonds are similar in energy and heavily mixed with the 6*d*-orbitals. However, the close proximity of the pre-edge feature associated with these orbitals to the white line inhibited a quantitative evaluation of Cl and Th orbital mixing.

In contrast, the pre-edge features for **5** were resolved from the white line and provide direct and quantitative experimental evidence for covalency in actinide ligand bonding. The intensity of the experimental resolved pre-edge features, indicate that the U-Cl bond contains approximately half the Cl 3*p* character as the analogous Ti, Zr, and Hf complexes. Moreover, the Cl K-edge XAS of **5** provides an opportunity to evaluate the relative roles of the 5*f*- vs. 6*d*-orbital in bonding, which represents a long-standing challenge in *f*-element chemistry. For example, the experimental data is consistent with the DFT analysis, and suggest that the low lying U 5*f*-orbitals are split in a 5-over-2 pattern and involved in covalent mixing with the Cl 3*p* oribitals. In addition, the experimental data indicates that the high lying U 6*d*-orbitals, which are split in the same 4-over-1 pattern as observed in **1 – 3**, provide the major covalent component for the U-Cl bond in $(C_5Me_5)_2UCl_2$.

The use of ligand K-edge XAS in conjunction with ground state and hybrid-DFT calculations provides a unique approach to probe electronic structure, bonding, and covalency in *f*-element compounds in comparison to *d*-block elements, which is not easily accessible by conventional spectroscopy. These results also offer a foundation with which to further explore covalency in actinide-ligand bonding, which is important for controlling 5*f*-element chemical reactivity and actinide physical properties. Current efforts are currently underway to expand the use of ligand K-edge XAS and DFT to evaluate compounds containing transuranic elements, where both 5*f*- and 6*d*-orbitals are expected to play a role in M-Cl bonding.

Acknowledgment.

Table 1. A comparison of experimental and calculated pre-edge peak energies (eV), intensities, and % Cl 3p character[a] for $(C_5R_5)_2MCl_2$ complexes (M = Ti, Zr, and Hf, R = H, Me).[a]

Compound	Peak 1				Peak 2				Peak 3			
	Energy	Int.	% Cl 3p	% Cl 3p	Energy	Int	% Cl 3p	% Cl 3p	Energy	Int	% Cl 3p	% Cl 3p
	exp.	exp.	exp.	calc.	exp.	exp.	exp.	calc.	exp.	exp.	exp.	cacl.
D_{2d}–Cs_2CuCl_4[35]	2820.20	0.53	7.53	7.53	–	–	–	–	–	–	–	–
$(C_5Me_5)_2TiCl_2$, **1**	2821.31	0.30	4	5	2822.31	1.48	21	11	–	–	–	–
$(C_5Me_5)_2ZrCl_2$, **2**	2822.41	0.51	7	5	2823.62	1.08	15	7	–	–	–	–
$(C_5Me_5)_2HfCl_2$, **3**	2822.86	0.62	9	5	2823.93	0.56	8	3	2824.56	0.35	5	4
$(C_5Me_5)_2ThCl_2$, **4**[b]	2825.58	1.02	14	9	–	–	–	–	–	–	–	–
$(C_5Me_5)_2UCl_2$, **5**	2821.17	0.05	1	3	2821.99	0.19	3	5	2823.44	0.40	6	4
$(C_5H_5)_2TiCl_2$, **6**[c]	2821.19	0.44	6	6	2822.24	1.37	19	14	–	–	–	–
$(C_5H_5)_2ZrCl_2$, **7**[40]	2822.37	0.65	9	6	2823.62	1.13	16	12	–	–	–	–
$(C_5H_5)_2HfCl_2$, **8**[40]	2822.82	0.65	9	6	2824.01	0.69	10	11	–	–	–	–

[a] The percent Cl 3p character is reported per M-Cl bond.
[b] Given the difficulty in resolving the pre-edge shoulder for **3**, caution must be taken when drawing conclusions based on the pre-edge peak intensity.
[c] Although compound **5** has been the focus of previous experimental and theoretical investigations,[36,40,53] the experimental values in Table **1** are from previous analyses made on samples that had been encapsulated in polystyrene,[40] and the calculated values were conducted in a similar fashion as those for compounds **2 – 4**.[40]

Table 2. A comparison of experimental and calculated total pre-edge peak intensities and total % Cl $3p$ character[a] for $(C_5R_5)_2MCl_2$ complexes (M = Ti, Zr, Hf, Th, and U).[a]

Compound	Int.	% Cl $3p$	% Cl $3p$
	exp.	exp.	calc.
D_{2d}-Cs_2CuCl_4[35]	0.54	7.5	–
$(C_5Me_5)_2TiCl_2$, **1**	1.78	25	16
$(C_5Me_5)_2ZrCl_2$, **2**	1.59	23	14
$(C_5Me_5)_2HfCl_2$, **3**	1.53	22	12
$(C_5Me_5)_2ThCl_2$, **4**[b]	1.02	14	9
$(C_5Me_5)_2UCl_2$, **5**	0.64	9	12
$(C_5H_5)_2TiCl_2$, **6**[c]	1.81	25	20
$(C_5H_5)_2ZrCl_2$, **7**[40]	1.78	25	18
$(C_5H_5)_2HfCl_2$, **8**[40]	1.34	19	17
$(C_5H_5)_2ThCl_2$, **9**	–	–	17
$(C_5H_5)_2UCl_2$, **10**	–	–	16

[a]The percent Cl $3p$ character is reported per M-Cl bond.
[b]Given the difficulty in resolving the pre-edge shoulder for **3**, caution must be taken when drawing conclusions based on the pre-edge peak intensity.
[c]Although compound **5** has been the focus of previous experimental and theoretical investigations,[36,40,54] the experimental values in Table **2** are from previous analyses made on samples that had been encapsulated in polystyrene,[39] and the calculated values were conducted in a similar fashion as those for compounds **2 – 4**.[39]

Table 3. Orbital composition for the five metal d-based orbitals in $(C_5Me_5)_2MCl_2$ (M = Ti, Zr, and Hf).

	MO Label (Symmetry)					
	59 (1a$_1$) (LUMO)	60 (1b$_2$)	61 (1b$_1$)	62 (1a$_2$)	63 (2a$_1$)	Total
$(C_5Me_5)_2TiCl_2$, 1						
Energy (eV)	-2.14	-1.29	-1.17	-1.04	-0.86	
Total % Ti $3d$	79.4	57.2	70.4	68.4	72	347.4
Total % Ti $4p$	0.5	1.8	0.0	0.0	0.1	2.4
Total % Cl $3p$	9.8	13.5	1.8	1.3	5.4	31.8
Total % $(C_5Me_5)^{1-}$	10.3	27.5	27.8	30.3	22.5	118.4
$(C_5Me_5)_2ZrCl_2$, 2						
Energy (eV)	-1.73	-0.77	-0.30	0.00	0.11	
Total % Zr $4d$	71.9	49.2	67.7	63.3	60.3	312.4
Total % Zr $5p$	0.6	3.2	0.0	0.0	1.8	5.6
Total % Cl $3p$	9.8	8.2	2.4	2.4	5	27.8
Total % $(C_5Me_5)^{1-}$	17.7	39.4	29.9	34.3	32.9	154.2
$(C_5Me_5)_2HfCl_2$, 3						
Energy (eV)	-1.41	-0.56	0.11	0.40	0.44	
Total % Hf $5d$	67.0	45.4	60.9	34.6	50.3	258.2
Total % Hf $6p$	1.0	2.8	0.4	2.1	0.3	6.6
Total % Cl $3p$	9.4	5.6	1.8	4.8	2.2	23.8
Total % $(C_5Me_5)^{1-}$	22.6	46.2	36.9	58.5	47.2	211.4

29

Table 4. Orbital composition for the twelve 5*f* and 6*d*-based orbitals in $(C_5R_5)_2AnCl_2$ (M = Th and U; R = H, Me).

$(C_5H_5)_2ThCl_2$, 9

MO Label	68 (LUMO)	69	70	71	72	73	74	75	76	77	78	80	Total	Summation (68-75)
Energy (eV)	-1.78	-1.68	-1.46	-1.41	-1.19	-1.00	-0.90	-0.71	0.33	0.57	0.58	1.45		
Total % Th 5*f*	60.9	50.4	78.8	78.9	78.6	93.1	83.1	41.3	21.9	22.2	30.2	1.6	641.0	--
Total % Th 6*d*	13.5	25.3	6.9	3.8	8.3	1.6	10.6	41.7	51.9	37.3	26.3	61.9	289.1	--
Total % Cl 3*p*	0.8	2.5	0.9	8.6	4.3	3.6	3.2	9.5	3.3	4.8	9.6	10	61.1	16.7
Total % $(C_5H_5)^{1-}$	24.7	21.7	13.4	8.7	8.8	1.5	3.0	7.1	22.9	35.5	33.5	26.3	207.1	--

$(C_5Me_5)_2ThCl_2$, 4

MO Label	108 (LUMO)	109	110	111	112	133	114	115	116	117	118	119	Total	Summation (108-115)
Energy (eV)	-1.26	-1.20	-0.97	-0.91	-0.65	-0.40	-0.32	-0.17	0.81	0.87	1.01	1.16		
Total % Th 5*f*	52.3	39.4	67.3	76.5	76.9	92.0	85.0	56.9	24.9	43.8	24.0	16.8	655.8	--
Total % Th 6*d*	22.1	36.5	8.3	7.5	5.8	2.2	8.7	30.3	5.5	17.5	46.1	35.7	226.2	--
Total % Cl 3*p*	1.2	1.7	0.6	0.0	3.4	2.9	2.2	5.8	5.3	9.6	1.6	0.6	34.9	17.8
Total % $(C_5Me_5)^{1-}$	24.1	22.3	23.7	16.0	13.9	2.5	3.8	6.4	64.1	28.3	28.1	46.9	280.1	--

$(C_5H_5)_2UCl_2$, 10

	Primarily 5f							Primarily 6d					Total	Summation (68-75)
	68 (SOMO-1)	69 (SOMO)	70 (LUMO)	71	72	73	74	75	76	77	78	79		
Energy (eV)	-6.84	-6.51	-3.32	-3.15	-2.90	-2.77	-2.56	-1.15	-0.13	0.10	0.49	1.18		
Total % U 5f	92.7	70.6	92.4	87.3	89.8	86.7	85.0	4.4	7.3	4.2	4.2	1.8	626.4	—
Total % U 6d	1.3	4.6	1.7	1.8	2.3	4.4	5.5	59.1	31.4	51.9	38.7	34.8	237.5	—
Total % Cl 3p	1.2	9.6	0.9	2.6	2.8	2.7	2.0	9.1	6.8	1.8	2.6	44.7	86.8	30.8
Total % $(C_5H_5)^{1-}$	4.7	15.1	5.0	8.3	5.0	6.2	7.5	26.8	53.8	42.1	54.5	18.7	247.7	—

$(C_5Me_5)_2UCl_2$, 5

	Primarily 5f							Primarily 6d					Total	Summation (108-115)
	108 (SOMO-1)	109 (SOMO)	110 (LUMO)	111	112	133	114	115	116	117	118	119		
Energy (eV)	-5.93	-5.86	-2.73	-2.53	-2.35	-2.07	-1.93	-0.81	0.35	0.55	0.74	0.99		
Total % U 5f	44.1	12.3	89.2	88.4	88.4	84.5	87.1	2.5	10.9	4.9	5.0	3.7	521	—
Total % U 6d	6.2	2.9	2.9	2.9	3.3	5.0	4.3	61.7	30.1	18.7	37.5	29.9	205.4	—
Total % Cl 3p	3.6	2.1	1.5	2.5	2.7	1.5	1.8	7.3	1.3	2.4	1.9	1.3	29.9	23
Total % $(C_5Me_5)^{1-}$	45.1	80.5	6.4	6.2	5.6	8.6	6.7	27.9	9.3	60.4	55.4	65.1	377.2	—

References

(1)   Cotton, F. A.; Wilkinson, G.; Murillo, C. A. Bochmann, M. "Advanced Inorganic Chemistry" 6th Ed. John Wiley and Sons, Inc. New York, **1999**, pg. 633-635.

(2)   Crosswhite, H. M.; Crosswhite, H.; Carnall, W. T.; Paszek, A. P. *J. Chem. Phys.* **1980**, *72*, 5103

(3)   Glueckauf, E.; McKay, H. A. C. *Nature,* **1950**, *165*, 594.

(4)   Katzin, L. I. *Nature,* **1950**, *166*, 605.

(5)   Street, Jr, K; Seaborg, G. T. *J. Am. Chem. Soc.* **1950**, *72*, 2790.

(6)   Baker, E. C.; Halstead, G. W.; Raymond, K. N. *Struct. Bonding (Berlin)* **1976**, *25*, 23.

(7)   Raymond, K. N.; Eigenbrot Jr., C. W. *Acc. Chem. Res.* **1980**, *13*, 276.

(8)   Iversen, B. B.; Larsen, F. K.; Pinkerton, A. A.; Martin, A.; Darovsky, A.; Reynolds, P. A. *Inorg. Chem.* **1998**, *37*, 4559.

(9)   Choppin, G. R. *J. Alloys Comp.* **2002**, *344*, 55.

(10)   Prodan, I. D.; Scuseria, G. E.; Martin, R. L. *Phys. Rev. B.* **2007**, *76*, 033101.

(11)   Roger, M.; Belkhiri, L.; Arliguie, T.; Thuéry, P.; Boucekkine, A.; Ephritikhine, M. *Organometallics* **2008**, *27*, 33.

(12)   Ingram, K. I. M.; Tassell, M. J.; Gaunt, A. J.; Kaltsoyannis, N. *Inorg. Chem.* **2008**, *47*, 7824.

(13)   Gaunt, A. J.; Reilly, S. D.; Enriquez, A. E.; Scott, B. L.; Ibers, J. A.; Sekar, P.; Ingram, K. I. M.; Kaltsoyannis, N.; Neu, M. P. *Inorg. Chem.* **2008**, *47*, 29.

(14)   Beach, D. B.; Bomben, K. D.; Edelstein, N. M.; Eisenberg, D. C.; Jolly, W. L.; Shinomoto, R.; Streitwieser, A. Jr. *Inorg. Chem.* **1986**, *25*, 1735.

(15)   Bursten, B. E.; Strittmatter, R. J. *Angew. Chem. Int. Ed.* **1991**, *30*, 1069.

(16)   Denning, R. G.; Green, J. C.; Hutchings, T. E.; Dallera, C.; Tagliaferri, A.; Giarda, K.; Brookes, N. B.; Braicovich, L. *J. Chem. Phys.* **2002**, *117*, 8008.

(17)   O'Grady, E.; Kaltsoyannis, N. *J. Chem. Soc., Dalton Trans.,* **2002**, 1233.

(18)   Bercaw, J. E.; Marvich, R. H.; Bell, L. G.; Brintzinger, H. H. *J. Am. Chem. Soc.* **1972**, *94*, 1219.

(19)   Manriquez, J. M.; McAlister, D. R.; Rosenberg, E.; Shiller, A. M.; Williamson, K. L.; Chan, S. I.; Bercaw, J. E. *J. Am. Chem. Soc.* **1978**, *100*, 3078.

(20)   Roddick, D. M.; Fryzuk, M. D.; Seidler, P. F.; Hillhouse, G. L.; Bercaw, J. E. *Organometallics* **1985**, *4*, 97.

(21)   Manriquez, J. M.; Fagan, P. J.; Marks, T. J.; Vollmer, S. H.; Day, C. S.; Day, V. W. *J. Am. Chem. Soc.* **1979**, *101*, 5075.

(22)   Fagan, P. J.; Manriquez, J. M.; Maatta, E. A.; Seyam, A. M.; Marks, T. J. *J. Am. Chem. Soc.* **1981**, *103*, 6650.

(23)   Kanellakopulos, B.; Aderhold, C.; Dornberger, E. *J. Organomet. Chem.* **1974**, *66*, 447.

(24)   Ernst, R. D.; Kennelly, W. J.; Day, C. S.; Day, V. W.; Marks, T. J. *J. Am. Chem. Soc.* **1979**, *101*, 2656.

(25)   Marks, T. J. *Prog. Inorg. Chem.* **1979**, *25*, 223.

(26)   Marks, T. J.; Ernst, R. D. In *Comprehensive Organometallic Chemistry*; Wilkinson, G., Stone, F. G. A., Abel, E. W., Eds.; Pergamon: Oxford, U. K. **1982**; Chapter 21, p 211.

(27)   Edelmann, F. T.; In *Comprehensive Organometallic Chemistry II*; Wilkinson G.; Stone, F. G. A., Abel, E. W.; Eds; Pergamon: Osford, U. K., **1995**; Chapter 2, p 131.

(28)   Alt, H. G.; Koppl, A. *Chem. Rev.* **2000**, *100*, 1205.

(29)   Möhring, P. C.; Coville, N. J. *Coord. Chem. Rev.* **2006**, *250*, 18.

(30)   Hedman, B.; Hodgson, K. O.; Solomon, E. I. *J. Am. Chem. Soc.* **1990**, *112*, 1643.

(31)   Shadle, S. E.; Hedman, B.; Hodgson, K. O.; Solomon, E. I. *Inorg. Chem.* **1994**, *33*, 4235.

(32)   Shadle, S. E.; Hedman, B.; Hodgson, K. O.; Solomon, E. I. *J. Am. Chem. Soc.* **1995**, *117*, 2259.

(33)   Glaser, T.; Hedman, B.; Hodgson, K. O.; Solomon, E. I. *Acc. Chem. Res.* **2000**, *33*, 859.

(34)   Szilagyi, R. K.; Bryngelson, P. A.; Maroney, M. J.; Hedman, B.; Hodgson, K. O.; Solomon, E. I. *J. Am. Chem. Soc.* **2004**, *126*, 3018.

(35)   Solomon, E. I.; Hedman, B.; Hodgson, K. O.; Dey, A.; Szilagyi, R. K. *Coord. Chem. Rev.* **2005**, *249*, 97.

(36)   DeBeer George, S.; Brant, P.; Solomon, E. I. *J. Am. Chem. Soc.* **2005**, *127*, 667.

(37)   DeBeer George, S.; Huang, K.-W.; Waymouth, R. M.; Solomon, E. I. *Inorg. Chem.* **2006**, *45*, 4468.

(38)   Delgado-Jaime, M. U.; Conrad, J. C.; Fogg, D. E.; Kennepohl, P. *Inorg. Chim. Acta.* **2006**, *359*, 3042.

(39)   Ray, K.; DeBeer George, S.; Solomon, E. I.; Wieghardt, K.; Neese, F. *Chem. Eur. J.* **2007**, *13*, 2783.

(40)   Kozimor, S. A.; Yang, P.; Batista, E. R.; Boland, K. S.; Burns, C. J.; Christensen, C. N.; Clark, D. L.; Conradson, S. D.; Hay, P. J.; Lezama, J. S.; Martin, R. L.; Schwarz, D. E.; Wilkerson, M. P.; Wolfsberg, L. E. *Inorg. Chem.* **2008**, *47*, 5365.

(41)   Harkins, S. B.; Mankad, N. P.; Miller, A. J. M.; Szilagyi, R. K.; Peters, J. C. *J. Am. Chem. Soc.* **2008**, *130*, 3478.

(42)   Adhikari, D.; Mossin, S.; Basuli, F.; Huffman, J. C.; Szilagyi, R. K.; Meyer, K.; Mindiola, D. J. *J. Am. Chem. Soc.* **2008**, *130*, 3676.

(43)   Petersen, J. L.; Lichtenberger, D. L.; Fenske, R. F.; Dahl, L. R. *J. Am. Chem. Soc.* **1975**, *97*, 6433.

(44)   Lauher, J. W.; Hoffmann, R. *J. Am. Chem. Soc.* **1976**, *98*, 1729.

(45)   Bursten, B. E.; Fang, A. *J. Am. Chem. Soc.* **1983**, *105*, 6495.

(46)   Bruce, M. R. M.; Kenter, A.; Tyler, D. R. *J. Am. Chem. Soc.* **1984**, *106*, 639.

(47)   Tatsumi, K.; Nakamura, A.; Hofmann, P.; Stauffert, P.; Hoffmann, R. *J. Am. Chem. Soc.* **1985**, *107*, 4440.

(48)   Bursten B. E.; Fang, A.; *Inorg. Chem. Acta* **1985**, *110*, 153.

(49)   Tatsumi, K.; Nakamura, A. *J. Am.Chem. Soc.* **1987**, *109*, 3195.

(50)   Pepper, M.; Bursten, B. E. *Chem. Rev.* **1991**, *91*, 719.

(51)   Green, J. C. *Chem. Soc. Rev.* **1998**, *27*, 263.

(52)   Zachmanoglou, C. E.; Docrat, A.; Bridgewater, B. M.; Parkin G.; Brandow, C. G.; Bercaw, J. E.; Jardine, C. N.; Lyall, M.; Green, J. C.; Keister, J. B. *J. Am. Chem. Soc.* **2002**, *124*, 9525.

(53)   Wang, X.; Chen, L.; Endou, A.; Kubo, M.; Miyamoto, A.; *J. Organomet. Chem.* **2003**, *678*, 156.

(54)   Casarin, M.; Finetti, P.; Vittadini, A.; Wang, F.; Ziegler, T. *J. Phys. Chem. A* **2007**, *111*, 5270.

(55)   Condorelli, G.; Fragalá, I.; Centineo, A.; Tondello, E. *J. Organomet. Chem.* **1975**, *87*, 311.

(56)   Fragalá, I.; Marks, T. J.; Fagan, P. J.; Manriquez, J. M. ; *J. Electron Spectrosc. Rel. Phen.* **1980**, *20*, 249.

(57)   Ciliberto, E.; Condorelli, G.; Fagan, P. J.; Manriquez, J. M.; Fragalá, I.; Marks, T. J.; *J. Am. Chem. Soc.* **1981**, *103*, 4755.

(58)   King, W. A.; Di Bella, S.; Gulino, A.; Lanza, G.; Fragalá, I. L.; Stern, C. L.; Marks, T. J. *J. Am. Chem. Soc.* **1999**, *121*, 355.

(59)   Helmholz, L. Kruh, R. F. *J. Am. Chem. Soc.* **1952**, *74*, 1176.

(60)   Gewirth, A. A.; Cohen, S. L.; Schugar, H. J.; Solomon, E. I. *Inorg. Chem.* **1987**, *26*, 1133.

(61)   Didziulis, S. V.; Cohen, S. L.; Gewirth, A. A.; Solomon, E. I. *J. Am. Chem. Soc.* **1988**, *110*, 250.

(62)   Neese, F.; Hedman, B.; Hodgson, K. O.; Solomon, E. I. *Inorg. Chem.* **1999**, *38*, 4854.

(63)   Shadle, S. E. Ph.D. Thesis Stanford University **1994**.

(64)   George, G. N., EDG_FIT, Stanford Synchrotron Radiation Laboratory, Stanford Linear Accelerator Center, Stanford University, Stanford CA, USA.

(65)   Becke, A. D. *J. Chem. Phys.* **1993**, *98*, 5648.

(66)   Gaussian D.01, Frisch, M. J.; Trucks, G. W.; Schlegel, H. B.; Scuseria, G. E.; Robb, M. A.; Cheeseman, J. R.; J.A. Montgomery, J.; Vreven, T.; Kudin, K. N.; Burant, J. C.; Millam, J. M.; Iyengar, S. S.; Tomasi, J.; Barone, V.; Mennucci, B.; Cossi, M.; Scalmani, G.; Rega, N.; Petersson, G. A.; Nakatsuji, H.; Hada, M.; Ehara, M.; Toyota, K.; Fukuda, R.; Hasegawa, J.; Ishida, M.; Nakajima, T.; Honda, Y.; Kitao, O.; Nakai, H.; Klene, M.; Li, X.; Knox, J. E.; Hratchian, H. P.; Cross, J. B.; Bakken, V.; Adamo, C.; Jaramillo, J.; Gomperts, R.; Stratmann, R. E.; Yazyev, O.; Austin, A. J.; Cammi, R.; Pomelli, C.; Ochterski, J. W.; Ayala, P. Y.; Morokuma, K.; Voth, G. A.; Salvador, P.; Dannenberg, J. J.; Zakrzewski, V. G.; Dapprich, S.; Daniels, A. D.; Strain, M. C.; Farkas, O.; Malick, D. K.; Rabuck, A. D.; Raghavachari, K.; Foresman, J. B.; Ortiz, J. V.; Cui, Q.; Baboul, A. G.; Clifford, S.; Cioslowski, J.; Stefanov, B. B.; Liu, G.; Liashenko, A.; Piskorz, P.; Komaromi, I.; Martin, R. L.; Fox, D. J.; Keith, T.; Al-Laham, M. A.; Peng, C. Y.; Nanayakkara, A.; Challacombe, M.; Gill, P. M. W.; Johnson, B.; Chen, W.; Wong, M. W.; Gonzalez, C.; Pople, J. A., Gaussian Inc., Wallingford, CT, 2004.

(67)   Kuchle, W.; Dolg, M.; Stoll, H.; Preuss, H. *J. Chem. Phys.* **1994**, *100*, 7535.

(68)   Clark, A. E.; Martin, R. L.; Hay, P. J.; Green, J. C.; Jantunen, K. C.; Kiplinger, J. L. *J. Phys. Chem. A.* **2005**, *109*, 5481.

(69)   Bi, S, Lin, Z. Jordan, R. F. *Organometallics* **2004**, *23*, 4882.

(70)   Hay, P. J., *Organometallics* **2007**, 26, 4424.

(71)   Karttunen, V. A.; Linnolahti, M.; Pakkanen, T. A.; Maaranen, J.; Pitkänen, P. *Theo.-Chem. Acc.* **2007**, *118*, 899.

(72)   Graves, C. R.; Yang, P.; Kozimor, S. A.; Vaughn, A. E.; Clark, D. L.; Conradson, S. D.; Schelter, E. J.; Scott, B. L.; Thompson, J. D.; Hay, P. J.; Morris, D. E.; Kiplinger, J. L. *J. Am. Chem. Soc.* **2008**, *130*, 5272.

(73)   Martin, R. L.; Shirley, D. A., Many-electron theory of Photoemission. In *Electron Spectroscopy, Theory, Techniques and Applications*; Academic Press: New York, 1977; Vol. 1, p 75.

(74)   Clark, D. L.; Conradson, S. D.; Donohoe, R. J.; Keogh, D. W.; Morris, D. E.; Palmer, P. D.; Rogers, R. D.; Tait, C. D. *Inorg. Chem.* **1999**, *38*, 1456.

(75)   Conradson, S. D.; Manara, D.; Wastin, F.; Clark, D. L.; Lander, G. H.; Morales, L. A.; Rebizant, J.; Rondinella, V. V. *Inorg. Chem.* **2004**, *43*, 6922.

(76)   Strittmatter, R. J.; Bursten, B. E. *J. Am. Chem. Soc.* **1991**, *113*, 552.

(77)   Boerrigter, P. M.; Baerends, E. J.; Snijders, J. G. *Chem. Phys.* **1988**, 122, 357.

Supporting Information for

Trends in Covalency for d– and f–Element Metallocene Dichlorides Identified Using Chlorine K–Edge X–Ray Absorption Spectroscopy and Time Dependent–Density Functional Theory

Stosh A. Kozimor, Ping Yang, Enrique R. Batista, Kevin S. Boland, Carol J. Burns, David L. Clark,* Steven D. Conradson,* P. Jeffrey Hay, Richard L. Martin,* Marianne P. Wilkerson, Laura E. Wolfsberg

Los Alamos National Laboratory, Los Alamos, New Mexico 87545 (U.S.A.)

Received XXX, 2007, E-mail: dlclark@lanl.gov

Figure S1. A plot of normalized intensity vs. energy for the Cl K-edge X-ray absorption spectrum of $(C_5Me_5)_2TiCl_2$, **1**, that had been encapsulated in polystyrene; the experimental data (black), the curve fit (red dashes), and the functionals used to generate the fit (orange, blue, maroon, aqua, brown, and green).

Figure S2. A plot of normalized intensity vs. energy for the Cl K-edge X-ray absorption spectrum of $(C_5Me_5)_2ZrCl_2$, **2**, that had been encapsulated in polystyrene; the experimental data (black) the curve fit, (red dashes), and the functionals used to generate the fit (orange, blue, maroon, aqua, brown, and green).
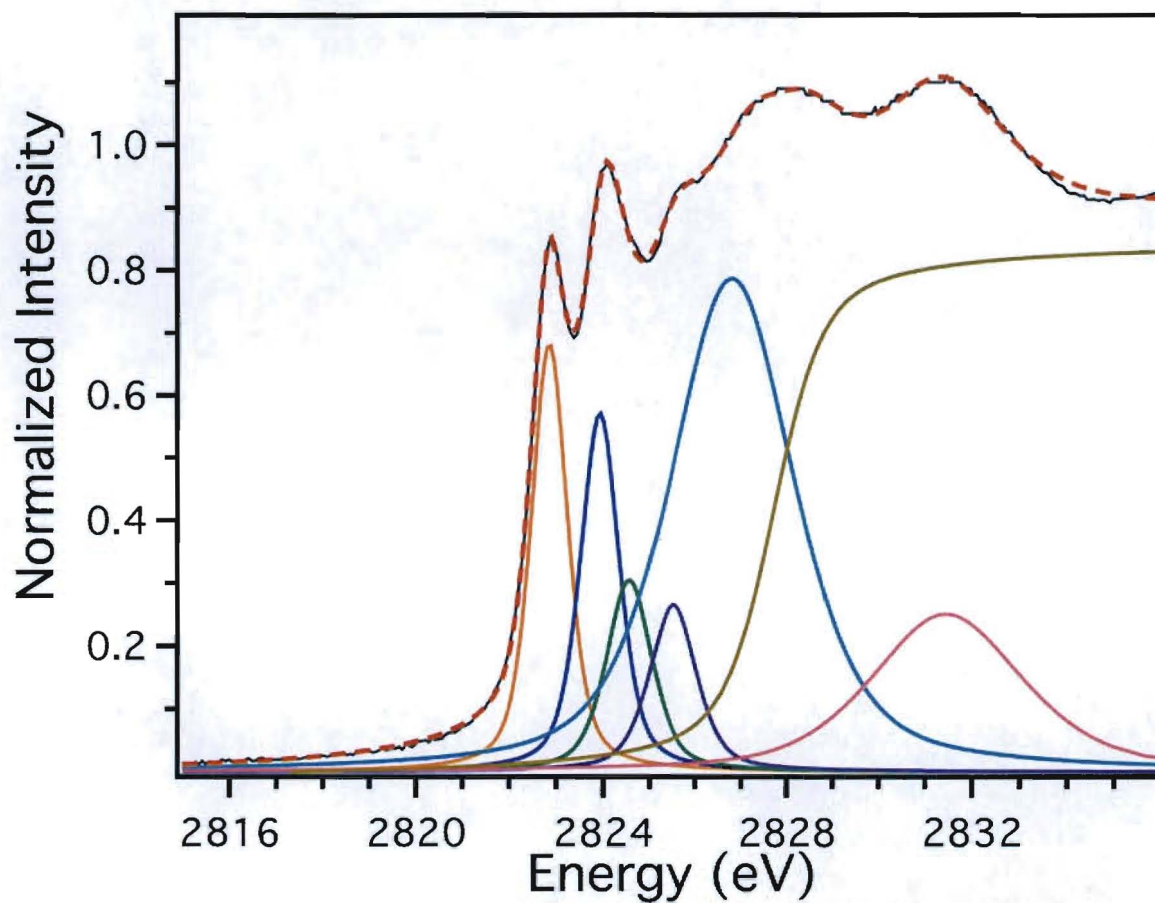
Figure S3. A plot of normalized intensity vs. energy for the Cl K-edge X-ray absorption spectrum of $(C_5Me_5)_2HfCl_2$, **3,** that had been encapsulated in polystyrene; the experimental data (black), the curve fit (red dashes), and the functionals used to generate the fit (orange, blue, purple, aqua, brown, and pink).
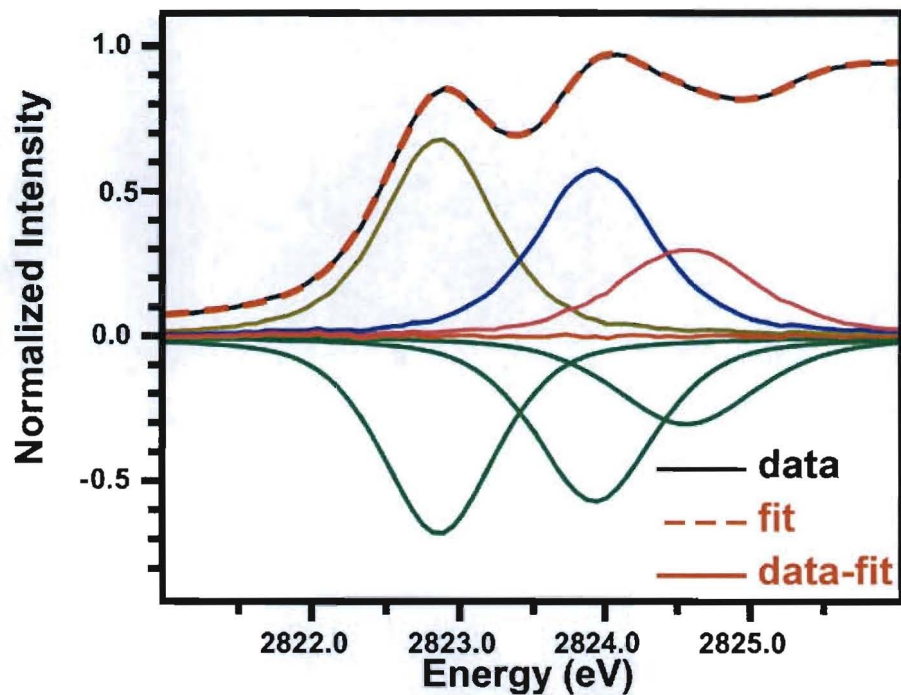
Figure S4. A plot of normalized intensity vs. energy for the Cl K-edge X-ray absorption spectrum with the experimental data (black line), curve fit (red dashes), residual data (red line), residual peaks (brown, blue, and pink), and negative amplitudes of the pre-edge pseudo-Voight functions (green) for polystyrene film samples of $(C_5Me_5)_2HfCl_2$, **3**.
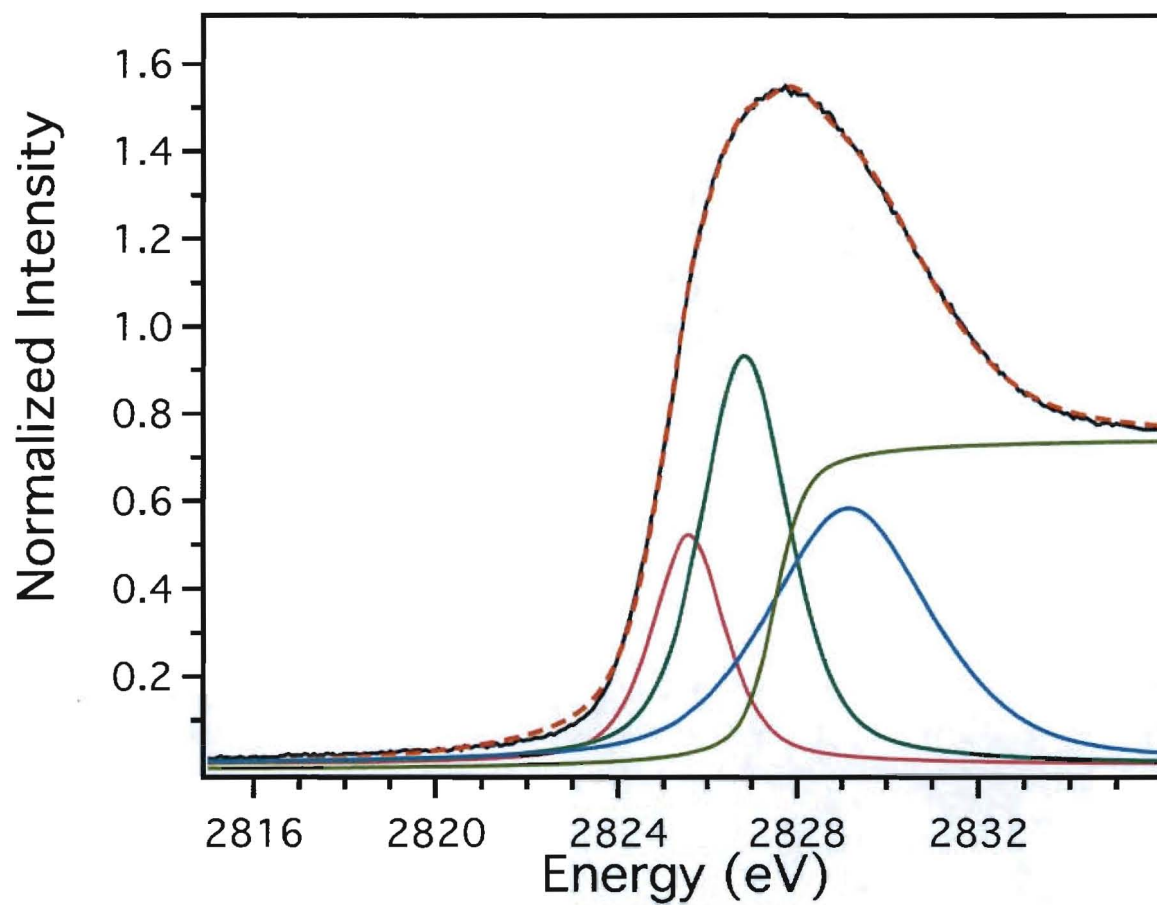
Figure S5. A plot of normalized intensity vs. energy for the Cl K-edge X-ray absorption spectrum of $(C_5Me_5)_2ThCl_2$, **4**, that had been encapsulated in polystyrene; the experimental data (black), the curve fit (red dashes), and the functionals used to generate the fit (maroon, green, brown, and aqua).
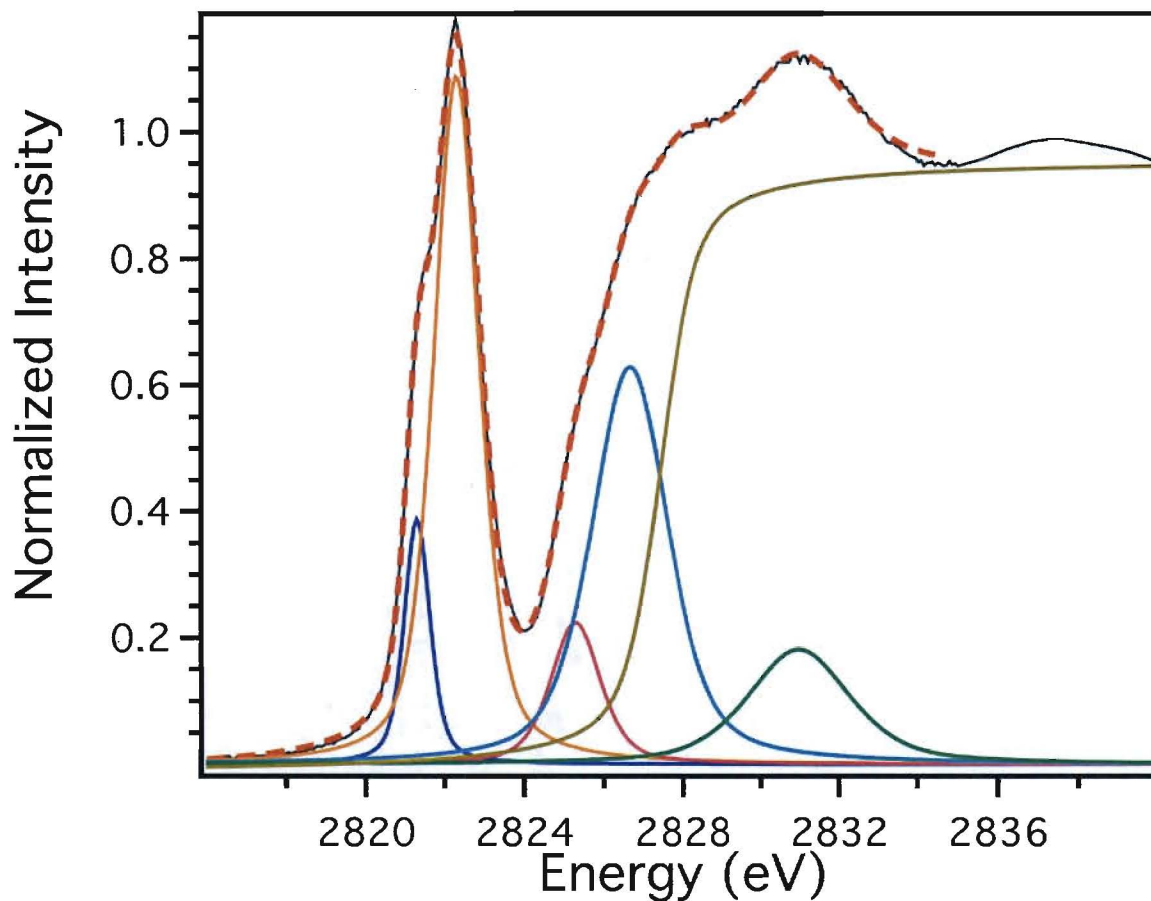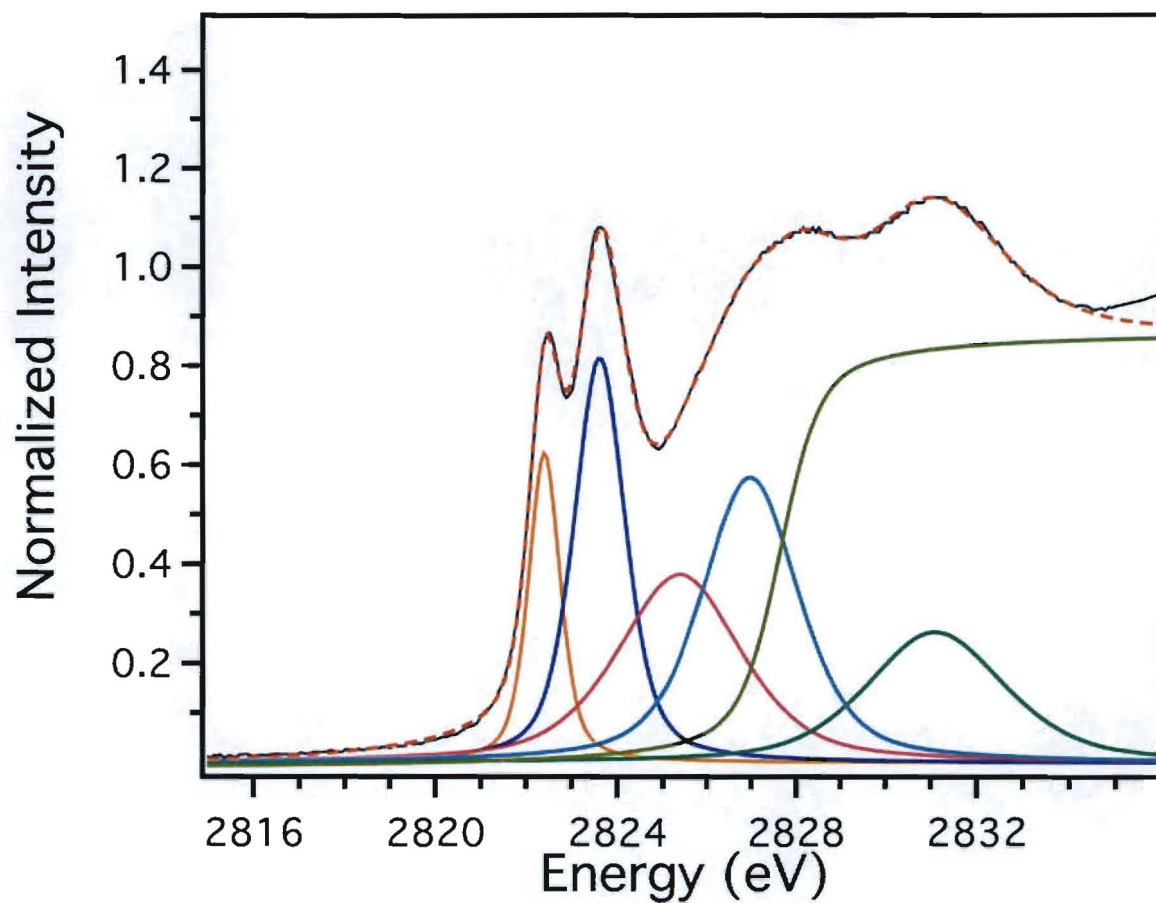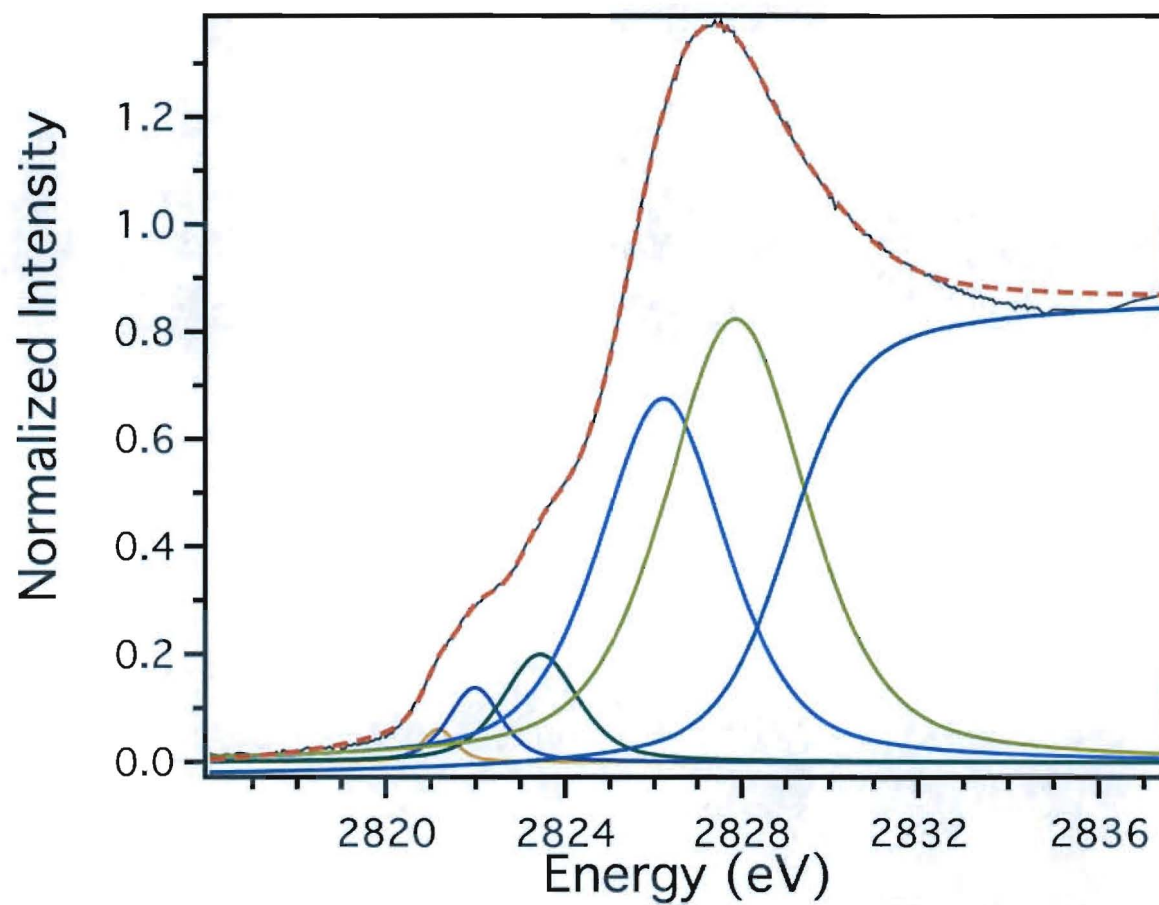
Figure S6. A plot of normalized intensity vs. energy for the Cl K-edge X-ray absorption spectrum of $(C_5Me_5)_2UCl_2$, **5**, that had been encapsulated in polystyrene; the experimental data (black), the curve fit (red dashes), and the functionals used to generate the fit (orange, blue, green, aqua, brown, and navy).

Table S1. The average experimental bond lengths and the calculated bond lengths for the optimized structures of $(C_5Me_5)_2MCl_2$ (M = Ti, **1**; Zr, **2**; Hf, **3**; Th, **4**; and U, **5**).

	M-Cl (Å)		M-C$_{centroid}$ (Å)	
	Expt. (ave.)	Calc.	Expt. (ave.)	Calc.
$(C_5Me_5)_2TiCl_2$	2.349	2.363	2.128	2.153
$(C_5Me_5)_2ZrCl_2$	2.462	2.476	2.262	2.300
$(C_5Me_5)_2HfCl_2$	--	2.467	--	2.293
$(C_5Me_5)_2ThCl_2$	2.601	2.660	2.532	2.561
$(C_5Me_5)_2UCl_2$	2.585	2.604	2.465	2.485

Table S2. The pre-edge peak splitting for $(C_5Me_5)_2MCl_2$ (M = Ti, **1**; Zr, **2**; Hf, **3**; Th, **4**; and U, **5**).

	Pre-edge peak splitting (eV)	
	Expt.	Calc.
$(C_5Me_5)_2TiCl_2$	--	0.80
$(C_5Me_5)_2ZrCl_2$	--	1.10
$(C_5Me_5)_2HfCl_2$	--	1.10
$(C_5Me_5)_2ThCl_2$	--	--
$(C_5Me_5)_2UCl_2$	--	3.50 & 1.60

Table S3. The charge distribution (NBO Analysis) for $(C_5Me_5)_2MCl_2$ (M = Ti, **1**; Zr, **2**; Hf, **3**; Th, **4**; and U, **5**).

	M Natural Charges	Cl Natural Charges	Cp* ring Natural Charges
$(C_5Me_5)_2TiCl_2$	+ 1.312	- 0.435	- 0.221
$(C_5Me_5)_2ZrCl_2$	+ 1.328	- 0.420	- 0.244
$(C_5Me_5)_2HfCl_2$	+ 1.558	- 0.432	- 0.347
$(C_5Me_5)_2ThCl_2$	+ 1.701	- 0.432	- 0.418
$(C_5Me_5)_2UCl_2$	+ 1.516	- 0.418	- 0.340

Table S4. The average experimental bond lengths and the calculated bond lengths for the optimized structures of $(C_5H_5)_2MCl_2$ (M = Ti, **6**; Zr, **7**; Hf, **8**; Th, **9**; and U, **10**).

	M-Cl (Å)		M-$C_{centroid}$ (Å)	
	Expt. (ave.)	Calc.	Expt. (ave.)	Calc.
$(C_5H_5)_2TiCl_2$	2.356	2.355	2.121	2.085
$(C_5H_5)_2ZrCl_2$	2.451	2.468	2.197	2.257
$(C_5H_5)_2HfCl_2$	2.424	2.459	2.182	2.252
$(C_5H_5)_2ThCl_2$	--	2.643	--	2.544
$(C_5H_5)_2UCl_2$	--	2.589	--	2.442

Table S5. The pre-edge peak splitting for $(C_5H_5)_2MCl_2$ (M = Ti, **6**; Zr, **7**; Hf, **8**; Th, **9**; and U, **10**).

	Pre-edge peak splitting (eV)	
	Expt.	Calc.
$(C_5H_5)_2TiCl_2$	0.9	0.9
$(C_5H_5)_2ZrCl_2$	1.26	1.15
$(C_5H_5)_2HfCl_2$	1.19	1.10
$(C_5H_5)_2ThCl_2$	--	--
$(C_5H_5)_2UCl_2$	--	3.70 & 1.70

Table S6. The charge distribution (NBO Analysis) for $(C_5H_5)_2MCl_2$ (M = Ti, **6**; Zr, **7**; Hf, **8**; Th, **9**; and U, **10**).

	M Natural Charges	Cl Natural Charges	Cp ring Natural Charges
$(C_5H_5)_2TiCl_2$	+ 0.881	- 0.370	- 0.071
$(C_5H_5)_2ZrCl_2$	+ 1.215	- 0.395	- 0.212
$(C_5H_5)_2HfCl_2$	+ 1.475	- 0.414	- 0.324
$(C_5H_5)_2ThCl_2$	+ 1.602	- 0.382	- 0.419
$(C_5H_5)_2UCl_2$	+ 1.384	- 0.368	- 0.324

Table S7. The orbital compositions for representative occupied and unoccupied orbitals in $(C_5Me_5)_2TiCl_2$, **1.**

MO Label	Energy (eV)	Ti 3d	Ti 4p	Cl 3p	Cp* total
103	-0.86	72.0	0.1	5.4	22.5
102	-1.04	68.4	0.0	1.3	30.3
101	-1.17	70.4	0.0	1.8	27.8
100	-1.29	57.2	1.8	13.5	27.5
99 LUMO	-2.14	79.4	0.5	9.8	10.3
98 HOMO	-5.72	13.6	0.1	17.8	68.5
97	-6.05	14.5	0.9	23.2	61.4
96	-6.07	10.2	3.6	13.4	72.8
95	-6.49	16.6	4.7	0.9	77.8
94	-7.10	2.9	2.8	85.9	8.4
93	-7.61	10.2	0.0	67.9	21.9
92	-7.64	0.2	1.4	75.0	23.4
91	-7.91	7.3	0.3	87.2	5.2
90	-8.42	7.9	0.6	75.1	16.4
89	-8.44	13.6	0.0	79.3	7.1

Table S8. The orbital compositions for representative occupied and unoccupied orbitals in (C$_5$Me$_5$)$_2$ZrCl$_2$, **2.**

MO Label	Energy (eV)	Zr 4d	Zr 5p	Cl 3p	Cp* total
103	0.11	60.3	1.8	5.0	32.9
102	0.00	63.3	0.0	2.4	34.3
101	-0.30	67.7	0.0	2.4	29.9
100	-0.77	49.2	3.2	8.2	39.4
99 LUMO	-1.73	71.9	0.6	9.8	17.7
98 HOMO	-5.95	11.0	0.2	11.4	77.4
97	-6.07	6.0	4.9	4.0	85.1
96	-6.28	13.6	0.1	18.0	68.3
95	-6.51	13.4	4.4	1.4	80.8
94	-7.50	0.8	1.6	93.6	4.0
93	-7.87	9.3	0.0	74.4	16.3
92	-7.90	6.5	0.3	81.2	12.0
91	-8.21	7.4	0.1	88.9	3.6
90	-8.67	6.7	0.3	76.7	16.3
89	-8.76	10.5	0.3	81.5	7.7

Table S9. The orbital compositions for representative occupied and unoccupied orbitals in $(C_5Me_5)_2HfCl_2$, **3.**

MO Label	Energy (eV)	Hf 5d	Hf 6p	Cl 3p	Cp* total
103	0.44	50.3	0.3	2.2	47.2
102	0.40	34.6	2.1	4.8	58.5
101	0.11	60.9	0.4	1.8	36.9
100	-0.56	45.4	2.8	5.6	46.2
99 LUMO	-1.41	67.0	1.0	9.4	22.6
98 HOMO	-5.92	10.0	0.1	10.4	79.5
97	-6.08	5.8	4.8	3.8	85.6
96	-6.24	12.7	0.1	16.0	71.2
95	-6.50	12.5	4.4	1.0	82.1
94	-7.58	0.7	1.6	93.6	4.1
93	-7.93	7.9	0.0	76.2	15.9
92	-7.98	3.9	3.0	81.5	11.6
91	-8.29	7.4	0.9	87.8	3.9
90	-8.79	6.7	0.2	68.0	25.1
89	-8.83	9.4	0.0	79.2	11.4

Table S10. The orbital compositions for representative occupied and unoccupied orbitals from the geometry optimized calculation for $(C_5H_5)_2ThCl_2$, **9**.

MO Label	Energy (eV)	Th 5f	Th 6d	Th 7s, 7p	Cl 3p	Cp total
81	1.47	1.2	0.7	0.0	85.8	12.3
80	1.45	1.6	61.9	0.2	10.0	26.3
79	0.75	11.5	6.6	0.1	69.8	12.0
78	0.58	30.2	26.3	0.4	9.6	33.5
77	0.57	22.2	37.3	0.2	4.8	35.5
76	0.33	21.9	51.9	0.0	3.3	22.9
75	-0.71	41.3	41.7	0.4	9.5	7.1
74	-0.90	83.1	10.6	0.1	3.2	3.0
73	-1.00	93.1	1.6	0.2	3.6	1.5
72	-1.19	78.6	8.3	0.0	4.3	8.8
71	-1.41	78.9	3.8	0.0	8.6	8.7
70	-1.46	78.8	6.9	0.0	0.9	13.4
69	-1.68	50.4	25.3	0.1	2.5	21.7
68 LUMO	-1.78	60.9	13.5	0.1	0.8	24.7
67 HOMO	-6.96	3.1	1.9	2.2	5.9	86.9
66	-6.99	7.1	4.8	0.3	3.8	84.0
65	-7.28	4.2	9.0	0.0	11.8	75.0
64	-7.37	0.0	9.5	1.7	6.4	82.4
63	-8.50	2.5	0.1	0.6	96.2	0.6
62	-8.71	1.1	3.8	0.5	91.0	3.6
61	-8.87	1.0	8.2	0.0	82.3	8.5
60	-8.89	0.4	7.4	0.4	88.3	3.5
59	-9.31	1.8	11.1	0.9	81.5	4.7
58	-9.36	2.3	7.8	0.9	82.8	6.2
57	-10.54	0.2	4.1	3.8	0.0	91.9

Table S11. The orbital compositions for representative occupied and unoccupied orbitals from the geometry optimized calculation for $(C_5Me_5)_2ThCl_2$, **4.**

MO Label	Energy (eV)	Th 5f	Th 6d	Th 7s, 7p	Cl 3p	Cp* total
125	2.06	2.3	0.0	0.1	45.5	52.1
121	1.38	1.2	11.9	0.3	20.2	66.4
120	1.37	2.5	3.3	0.0	22.8	71.4
119	1.16	16.8	35.7	0	0.6	46.9
118	1.01	24.0	46.1	0.2	1.6	28.1
117	0.87	43.8	17.5	0.8	9.6	28.3
116	0.81	24.9	5.5	0.2	5.3	64.1
115	-0.17	56.9	30.3	0.6	5.8	6.4
114	-0.32	85.0	8.7	0.3	2.2	3.8
113	-0.40	92.0	2.2	0.4	2.9	2.5
112	-0.65	76.9	5.8	0	3.4	13.9
111	-0.91	76.5	7.5	0	0	16.0
110	-0.97	67.3	8.3	0.1	0.6	23.7
109	-1.20	39.4	36.5	0.1	1.7	22.3
108 LUMO	-1.26	52.3	22.1	0.3	1.2	24.1
107 HOMO	-5.79	4.4	2.5	1.9	2.6	88.6
106	-6.05	2.6	9.0	1.2	2.6	84.6
105	-6.07	4.3	8.5	0.8	2.3	84.1
104	-6.25	3.0	12.7	0.0	5.0	79.3
103	-7.95	0.7	0.0	0.4	97.7	1.2
102	-8.05	0.0	1.3	1.1	86.1	11.5
101	-8.16	0.2	4.2	0.0	88.4	11.5
100	-8.33	0.0	4.9	0.6	90.2	4.3
99	-8.72	2.0	10.2	1.1	82.5	4.2
98	-8.75	2.1	8.2	0.9	78.3	10.5
97	-8.87	0.5	4.0	2.3	7.2	86.0

Table S12. The orbital compositions for representative occupied and unoccupied orbitals from the geometry optimized calculation for $(C_5H_5)_2UCl_2$, **10.**

MO Label	Energy (eV)	U 5f	U 6d	U 7s, 7p	Cl 3p	Cp total
82	1.56	2.6	21.8	0.2	11.3	64.1
81	1.48	0.1	0.2	0	88.8	10.9
80	1.18	1.8	34.8	0	44.7	18.7
79	0.49	4.2	38.7	0	2.6	54.5
78	0.24	2.4	0	98.0		
77	0.10	4.2	51.9	0.0	1.8	42.1
76	-0.13	7.3	31.4	0.7	6.8	53.8
75	-1.15	4.4	59.1	0.6	9.1	26.8
74	-2.56	85.0	5.5	0.0	2.0	7.5
73	-2.77	86.7	4.4	0.0	2.7	6.2
72	-2.90	89.8	2.3	0.1	2.8	5.0
71	-3.15	87.3	1.8	0	2.6	8.3
70 LUMO	-3.32	92.4	1.7	0	0.9	5.0
69	-6.51	70.6	4.6	0	9.6	15.2
68	-6.84	92.7	1.3	0.1	1.2	4.7
67	-7.09	10.2	1.7	2.2	7.3	78.6
66	-7.15	14.1	5.2	0.3	5.7	74.7
65	-7.45	2.1	10.1	1.5	7.5	78.8
64	7.49	21.9	7.5	0.1	10.8	59.7
63	-8.42	4.7	0.2	0.6	93.2	1.3
62	-8.67	2.2	4.2	0.5	87.5	5.6
61	-8.84	1.7	8.1	0	78.2	12.0
60	-8.84	1.1	7.1	0.3	87.2	4.3
59	-9.30	3.9	7.9	0.6	81.1	6.5
58	-9.32	5.9	10.1	0.4	78.8	4.8
57	-10.5	0.3	3.4	4.1	0	92.2

Table *S13*. The orbital compositions for representative occupied and unoccupied orbitals from the geometry optimized calculation for $(C_5Me_5)_2UCl_2$, **5.**

MO Label	Energy (eV)	U 5f	U 6d	U 7s, 7p	Cl 3p	Cp* total
125	2.07	0.4	**6.2**	0.4	39.9	53.1
121	1.52	0.2	10.0	1.0	22.5	66.3
120	1.42	0.3	0.7	0.5	28.2	70.3
119	0.99	3.7	29.9	0	1.3	65.1
118	0.74	5.0	37.5	0.2	1.9	55.4
117	0.55	4.9	18.7	13.6	2.4	60.4
116	0.35	10.9	30.1	1.3	9.3	48.4
115	-0.81	2.5	61.7	0.6	7.3	27.9
114	-1.93	87.1	4.3	0.1	1.8	6.7
113	-2.07	84.5	5.0	0.4	1.5	8.6
112	-2.35	88.4	3.3	0	2.7	5.6
111	-2.53	88.4	2.9	0	2.5	6.2
110 LUMO	-2.73	89.2	2.9	0.0	1.5	6.4
109	-5.86	12.3	2.9	2.2	2.1	80.5
108	-5.93	44.1	6.2	1.0	3.6	45.1
107	-6.04	43.6	3.3	0.3	4.1	48.7
106	-6.16	18.4	8.6	1.0	4.7	67.3
105	-6.25	59.7	5.3	0.2	0.7	34.1
104	-6.47	37.6	8.4	0.1	2.2	51.7
103	-7.93	3.4	0.1	0.4	94.8	1.3
102	-8.08	2.2	1.5	1.3	83.4	11.6
101	-8.16	2.9	3.9	0.1	85.1	8.0
100	-8.42	1.5	5.8	0.5	87.1	5.1
99	-8.77	3.2	7.8	0.7	74.2	14.1
98	-8.81	3.2	9.1	0.6	77.5	9.6
97	-8.86	1.3	3.7	2.2	8.1	84.7
96	-9.15	0.2	0.1	0	1.2	98.5